Molecular Cell

Article

A regulator of amino acid sensing links lipid peroxidation and lipid droplet-dependent antioxidant response

Graphical abstract

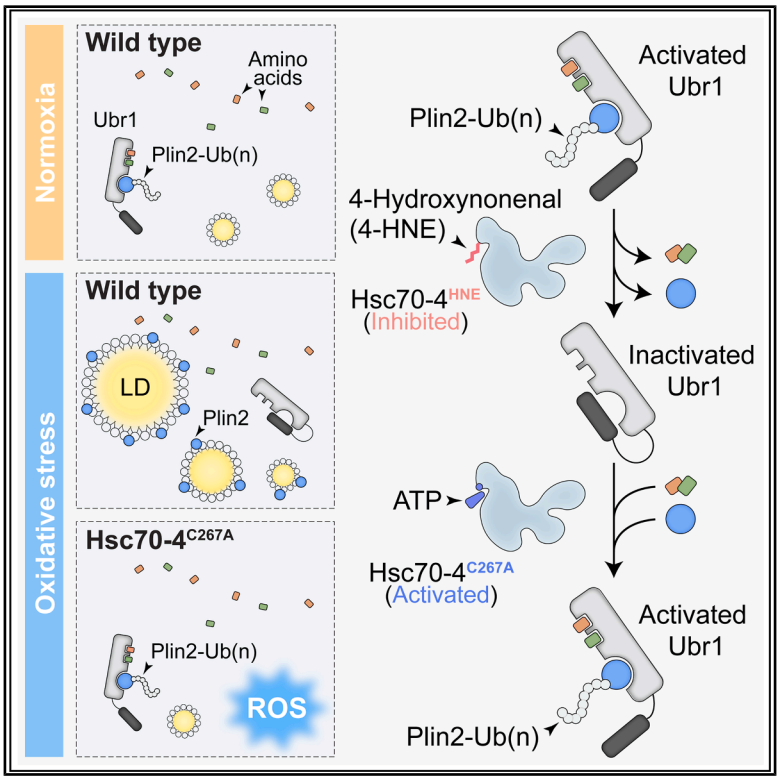

Highlights

- Oxidative stress induces glial lipid droplet accumulation by stabilizing Plin2
- During oxidative stress, amino acids cannot bind to or activate Ubr1 to degrade Plin2
- Hsc70-4 maintains Ubr1's amino-acid-binding ability and activity during normoxia
- Lipid peroxidation-derived 4-hydroxynonenal modifies and inactivates Hsc70-4

Authors

Jinhua Li, Yansong Zhang, Jingyu Peng, ..., Ming Ge, Min Liu, Alan Jian Zhu

Correspondence

geming@mail.ccmu.edu.cn (M.G.), liumin02@pku.edu.cn (M.L.), zhua@pku.edu.cn (A.J.Z.)

In brief

Li et al. find that the abrogation of amino acid sensing by Ubr1 induces lipid droplet accumulation as a protective response against oxidative stress. Lipid peroxidation during oxidative stress generates 4-hydroxynonenal, which directly inactivates Hsc70-4, the ATPase needed to maintain Ubr1 responsiveness and downstream control of lipolysis.

Li et al., 2025, Molecular Cell *85*, 3225–3240
September 4, 2025
https://doi.org/10.1016/j.molcel.2025.08.009

CellPress

Molecular Cell

CellPress

Article

A regulator of amino acid sensing links lipid peroxidation and lipid droplet-dependent antioxidant response

Jinhua Li,[1,7] Yansong Zhang,[1,2,3,7] Jingyu Peng,[1,6,7] Wei Yang,[4,7] Yanzhe Pan,[1] Ying Xu,[1] Jiayi Yao,[1] Siyuan Lin,[1] Yizhi Li,[1] Xinran Gu,[1] Wei Dong,[1] Xiang Yu,[1,2,5] Ming Ge,[4,*] Min Liu,[1,2,*] and Alan Jian Zhu[1,2,3,8,*]

[1]State Key Laboratory of Membrane Biology, School of Life Sciences, Peking University, Beijing 100871, China
[2]Peking-Tsinghua Center for Life Sciences, Academy for Advanced Interdisciplinary Studies, Peking University, Beijing 100871, China
[3]Peking University Chengdu Academy for Advanced Interdisciplinary Biotechnologies, Chengdu, Sichuan 610213, China
[4]Department of Neurosurgery, Beijing Children's Hospital, Capital Medical University, National Center for Children's Health, Beijing 100045, China
[5]Peking University McGovern Institute, Peking University, Beijing 100871, China
[6]Present address: Department of Stem Cell and Regenerative Biology, Harvard University and Harvard Stem Cell Institute, Cambridge, MA, USA
[7]These authors contributed equally
[8]Lead contact
*Correspondence: geming@mail.ccmu.edu.cn (M.G.), liumin02@pku.edu.cn (M.L.), zhua@pku.edu.cn (A.J.Z.)
https://doi.org/10.1016/j.molcel.2025.08.009

SUMMARY

Recent studies highlight the antioxidant role of lipid droplets (LDs) in shielding unsaturated lipids from peroxidation. While LDs accumulate during oxidative stress, the underlying mechanism remains unclear. Our previous research revealed that intracellular amino acids directly bind to and activate the E3 ubiquitin ligase Ubr1 to degrade Plin2, an LD protein inhibiting lipolysis. Here, we unexpectedly find that Ubr1's ability to bind to amino acids is inhibited during oxidative stress. Mechanistically, oxidative stress-induced lipid peroxidation blocks the activity of Hsc70-4, an ATPase that maintains the amino-acid-binding ability of Ubr1. 4-hydroxynonenal, a reactive product of lipid peroxidation, covalently modifies and inactivates Hsc70-4, leading to Ubr1 inactivation, Plin2 stabilization, and LD accumulation. Increased LDs minimize lipid peroxidation, thus protecting cells from oxidative damage and cell death. Together, we identify a regulator of amino acid sensing with redox-dependent activity, bridging the gap in understanding how lipid peroxidation stimulates LD-dependent antioxidant responses.

INTRODUCTION

Maintaining the homeostasis of reactive oxygen species (ROS) is crucial for the healthy growth and metabolic activity of aerobic organisms.[1,2] ROS serve as signaling molecules in various biological processes, including cell proliferation, differentiation, migration, and angiogenesis.[1–4] However, excessive ROS can lead to oxidative stress and lipid peroxidation, damaging essential biomolecules and ultimately leading to growth arrest or cell death.[1,5,6] Responding to this potential damage, cells have evolved diverse antioxidant defense mechanisms, including activation of antioxidant transcription factors, upregulation of glutathione (GSH) synthesis, and increase in nicotinamide adenine dinucleotide phosphate hydrogen (NADPH) production.[1,7,8]

Recent studies reveal an additional antioxidant defense mechanism involving glial lipid droplets (LDs) in the central nervous system. These previously overlooked organelles, known primarily for their role in lipid storage,[9,10] are emerging as integral players in cellular antioxidant defenses.[11–18] Rather than neutralizing ROS directly,[5,7,8] glial LDs protect polyunsaturated fatty acids (PUFAs) from lipid peroxidation, limiting the propagation of peroxidation chain reactions and preventing the unrestricted increases in ROS levels.[11–13] First observed in *Drosophila* glial cells, this conserved antioxidant function of LDs is critical for maintaining normal wake-sleep cycles[17] and for reducing oxidative damage in diseases associated with ROS, such as neurodegenerative disease.[14–16] Additionally, during tumor development, particularly in glioblastoma multiforme (GBM), the most prevalent and aggressive form of primary brain tumor, LD-dependent antioxidant activity alleviates oxidative damage, promoting tumor cell survival.[19–23] GBM cells contain a significant amount of LDs, and reducing their abundance in these cells can increase ROS levels, potentially leading to tumor cell death.[21] Nevertheless, the molecular mechanisms governing LD accumulation during oxidative stress and lipid peroxidation remain unresolved. Unveiling these mechanisms could unlock

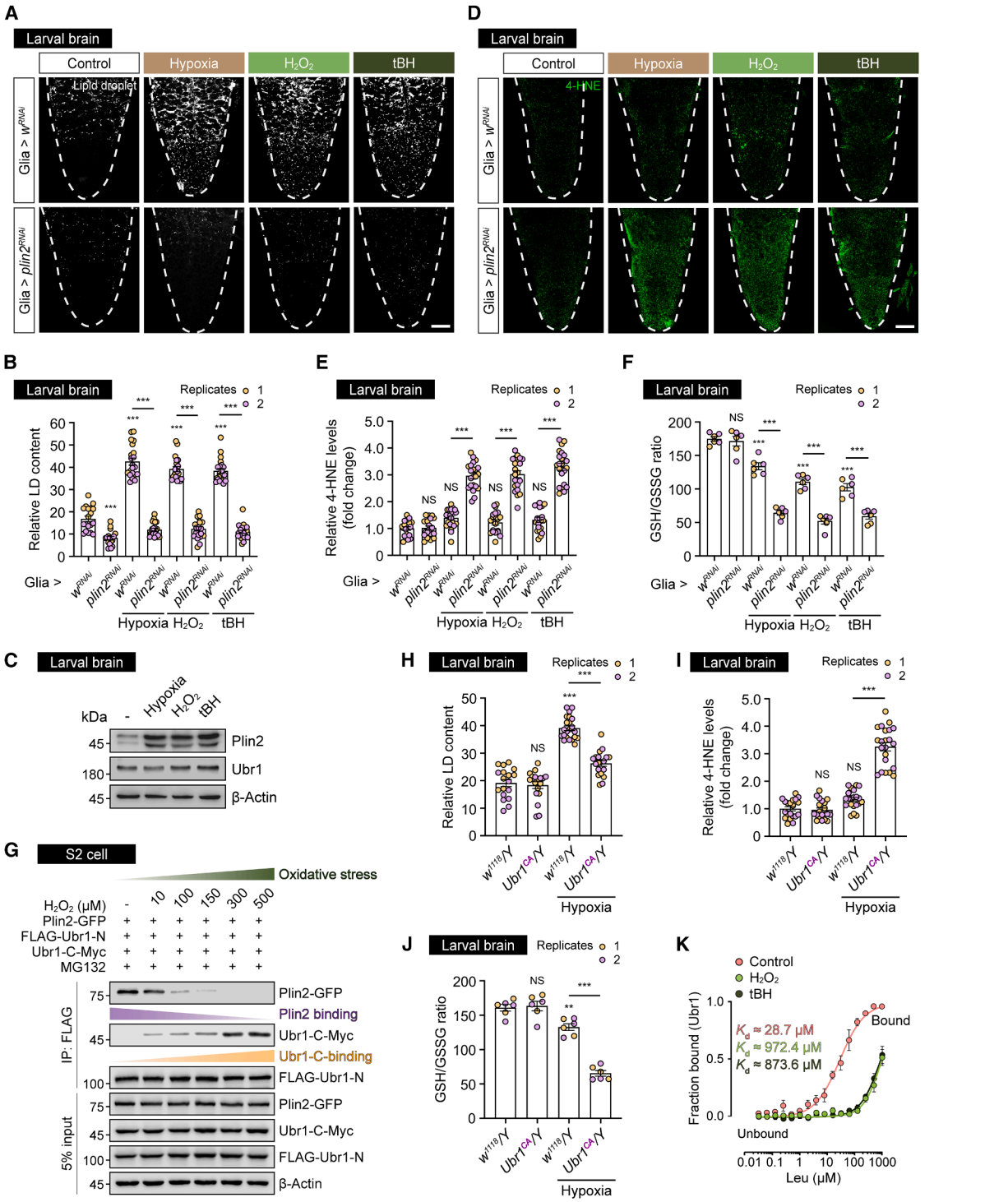

Figure 1. Ubr1's impaired amino-acid-binding ability promotes LD-dependent antioxidant responses in glial cells

(A and B) LDs (white) were stained with boron dipyrromethene (BODIPY) in the VNCs of *Drosophila* late-third instar larval brains of different genotypes (*repo* > *plin2*^{RNAi}, control: *repo* > *w*^{RNAi}), which were subjected to 16-h treatments of normoxia (20.9% oxygen) or three different oxidative stress conditions: hypoxia (2.5% oxygen), H_2O_2 (0.5% v/v), or tBH (100 mM). These conditions were applied consistently in all figures unless otherwise stated (A). Quantification of LD content (B). *n* = 19–22 larval brains from two independent experiments. One-way ANOVA, Tukey's multiple comparison tests. Note that *repo*-Gal4 was used as a driver to target expression specifically in larval glia. Scale bar, 50 μm.

(C) Immunoblotting analysis of Plin2 and Ubr1 in the brains of late-third instar larvae (genotype: *w*^{1118}/*Y*) subjected to normoxia, hypoxia, H_2O_2, or tBH treatment. β-actin served as a loading control.

(legend continued on next page)

new therapeutic strategies by exploiting LD dynamics in GBM treatment.

Our previous studies identified an amino-acid-induced ubiquitination pathway regulating LD homeostasis.[24] We showed that amino acids directly bind and activate the ubiquitin protein ligase E3 component n-recognin 1 (Ubr1), leading to perilipin 2 (Plin2) degradation, a protein that maintains LD stability and inhibits lipolysis. Conversely, reduced amino acid binding to Ubr1 decreased its activity, stabilizing Plin2 and causing LD accumulation. Thus, alterations in amino acid concentration or binding to Ubr1 may drive LD accumulation during oxidative stress, acting as an adaptive response to mitigate oxidative damage.

In this study, we show that oxidative stress induces glial LD accumulation by impairing Ubr1's amino-acid-binding affinity. Through a genetic screen, we identified the ATPase heat shock cognate protein 70-4 (Hsc70-4) as a critical regulator of Ubr1. Under oxidative stress, the lipid peroxidation product 4-hydroxynonenal (4-HNE) covalently modifies Hsc70-4 on the cysteine residue at position 267 (Cys267). This modification inactivates Hsc70-4 by impairing its ATP-binding ability, preventing Ubr1 from targeting Plin2 for degradation, and ultimately driving LD accumulation in glia. Strikingly, blocking 4-HNE modification of Hsc70-4 orthologs suppresses oxidative stress-induced LD accumulation, leading to elevated ROS in both *Drosophila* and mammalian glial cells. Importantly, increased 4-HNE modification of heat shock protein family A member 8 (HSPA8), the human ortholog of *Drosophila* Hsc70-4, correlates with advanced tumor grades and poor prognosis in glioma patients. Expressing a 4-HNE modification-resistant *HSPA8* variant sensitizes glioma cells susceptible to ROS-induced cell death and improves survival in a GBM mouse model. These findings link oxidative stress, lipid peroxidation, and LD accumulation through regulatable amino-acid-induced ubiquitination, highlighting HSPA8 activation as a promising therapeutic target in glioma treatment.

RESULTS

Oxidative stress inactivates Ubr1-mediated Plin2 degradation

We previously investigated the impact of environmental conditions on LD homeostasis during *Drosophila* development.[24] Here, we observed LD accumulation in brains of late-third instar larvae, particularly in glial cells of ventral nerve cords (VNCs) (Figure S1A), a tissue residing in a hypoxic microenvironment.[25] This phenotype was recapitulated in larvae exposed to chronic hypoxia or pro-oxidative agents, such as hydrogen peroxide (H_2O_2) and tert-butyl hydroperoxide (tBH) (Figures 1A, 1B, and S1A). These findings are consistent with recent reports of oxidative stress-induced glial LD accumulation,[11–16] prompting us to investigate the underlying mechanisms.

Plin2, an LD-stabilizing protein that inhibits lipolysis,[26] was significantly upregulated in larval brains under oxidative stress (Figure 1C). To investigate the significance of this upregulation, we knocked down *plin2* in various brain cell populations. Glial-specific *plin2* knockdown using *repo*-Gal4, a pan-glial driver expressed in nearly all VNC glial cells, abolished LD accumulation (Figures 1A and 1B). By contrast, *plin2* knockdown driven by *insc*-Gal4, targeting type-1 and type-2 neuroblasts (Figures S1B and S1C), or by $elav^{C155}$-Gal4, mainly expressed in neurons, had no effect (Figures S1B and S1C). These results demonstrate that Plin2 autonomously regulates oxidative stress-induced glial LD accumulation, with no detectable contribution from neuroblasts or neurons.

Under oxidative stress, ROS induce peroxidative damage to unsaturated lipids, generating 4-HNE, a lipid peroxidation product that can form covalent protein adducts.[11,27] To investigate lipid peroxidation levels in larval brains, we performed immunofluorescence staining for 4-HNE adducts. Despite elevated ROS under oxidative stress, only a modest increase in 4-HNE levels (Figures 1D and 1E) was observed, suggesting the presence of protective mechanisms in larval brains that mitigate lipid peroxidation. Since LDs shield unsaturated lipids against ROS attack,[11–13] we hypothesized that the oxidative stress-induced upregulation of Plin2 levels and LD contents in larval brains limit uncontrolled lipid peroxidation and maintain redox homeostasis. Indeed, glial-specific *plin2* knockdown under oxidative stress exacerbated the increase in 4-HNE levels (Figures 1D and 1E), indicating loss of peroxidation protection. This effect was accompanied by markedly increased ROS levels, as indicated by a reduced GSH-to-glutathione disulfide (GSSG) ratio (Figure 1F) and higher CellROX fluorescence (Figures S1D and S1E).

Despite increased Plin2 protein levels during oxidative stress (Figure 1C), its mRNA level remained unchanged (Figure S1F), indicating the presence of post-transcriptional regulation. We previously identified the ubiquitin ligase Ubr1 as a mediator of

(D and E) 4-HNE adducts (green) were stained with an anti-4-HNE antibody in the brains of late-third instar larvae of different genotypes (*repo* > $plin2^{RNAi}$, control: *repo* > w^{RNAi}), subjected to normoxia, hypoxia, H_2O_2, or tBH treatment (D). Quantification of 4-HNE adduct levels (E). n = 19–22 larval brains from two independent experiments. One-way ANOVA, Tukey's multiple comparison tests. Scale bar, 50 μm.

(F) The ratios of reduced glutathione to oxidized glutathione (GSH/GSSG) in the brains of late-third instar larvae of different genotypes (*repo* > $plin2^{RNAi}$, control: *repo* > w^{RNAi}) that were subjected to normoxia, hypoxia, H_2O_2, or tBH treatment. n = 6 biological samples (each containing 20 larval brains) from two independent experiments. One-way ANOVA, Tukey's multiple comparison tests.

(G) The interaction between the N-terminal fragment of *Drosophila* Ubr1 (Ubr1-N, amino acids 1–1,013) and Plin2, as well as the C-terminal fragment of Ubr1 (Ubr1-C, amino acids 1,532–1,824) in *Drosophila* S2 cells treated with H_2O_2 at the indicated concentrations for 1 h.

(H–J) LD content (H), 4-HNE adduct levels (I), and GSH/GSSG ratios (J) were quantified in the brains of late-third instar larvae of different genotypes ($Ubr1^{CA}$/Y, control: w^{1118}/Y). Larvae were exposed to hypoxia or normoxia for 16 h before harvest. n = 18–22 (H) or 20–22 (I) fly larval brains from two independent experiments (H and I). n = 6 biological samples (each containing 20 larval brains) from two independent experiments. One-way ANOVA, Tukey's multiple comparison tests.

(K) The binding affinity of *Drosophila* Ubr1 (purified from HEK293S cells; see also Figure S2J) to Leu was assessed using *in vitro* MST assays. Note that HEK293S cells were treated with 200 μM H_2O_2, 200 μM tBH, or left untreated for 1 h before harvest. Three independent experiments.

Data in all figures are shown as mean ± SEM. NS denotes not significant. $^*p < 0.05$, $^{**}p < 0.01$, $^{***}p < 0.001$.

Plin2 degradation via ubiquitination (Figure S1G).[24] Consistently, glial-specific *Ubr1* knockdown under normoxia increased Plin2 protein levels and LD contents in larval brains (Figures S1H–S1J). The autophagy-lysosome pathway also contributes to Plin2 degradation (Figure S1G).[28] Indeed, glial-specific knockdown of *Lamp1*, which encodes a lysosomal protein mediating protein degradation, mildly increased Plin2 and LD levels in larval brains under normoxia (Figures S1H–S1J). Intriguingly, under oxidative stress, *Ubr1* silencing no longer affected Plin2 or LD accumulation, whereas the autophagy-lysosome pathway remained active (Figures S1H–S1J). These findings imply regulation of Ubr1-mediated Plin2 degradation by oxidative stress.

Oxidative stress attenuates Ubr1's ability to bind amino acids and degrade Plin2

As the protein levels of Ubr1 were unaffected (Figure 1C), we investigated whether oxidative stress impaired its activity. Ubr1 contains a C-terminal auto-inhibitory domain that blocks substrate recognition, thereby suppressing its ubiquitin ligase activity.[24] In *Drosophila* Schneider's 2 (S2) cells exposed to increasing concentrations of H_2O_2, we observed a gradual decrease in the interaction between the N terminus of Ubr1 (Ubr1-N) and Plin2, concurrent with a gradual increase in binding of Ubr1-N to the C terminus of Ubr1 (Ubr1-C) (Figure 1G). This suggests that Ubr1 undergoes auto-inhibition during oxidative stress. To validate this, we used a constitutively active *Ubr1* knockin mutant (*Ubr1*^{CA}), in which cysteine residues at positions 1,703 and 1,706 critical for auto-inhibition were replaced with alanine (Ala).[24] *Ubr1*^{CA} knockin prevented oxidative stress-induced LD accumulation (Figures 1H and S2A) and increased 4-HNE and ROS levels in larval brains (Figures 1I, 1J, and S2B). Additionally, glial-specific *Ubr1*^{CA} expression prevented oxidative stress-induced LD accumulation, resulting in elevated 4-HNE and ROS levels (Figures S2C–S2G), thus confirming cell-autonomous regulation of Ubr1 activity in glial cells during antioxidant response.

Ubr1 activity depends on amino acid binding through two pockets.[29] The UBR (ubiquitin protein ligase E3 component n-recognin)-box-1 domain specifically binds three basic amino acids, including arginine (Arg), histidine (His), and lysine (Lys). The UBR-box-2 domain recognizes four bulky hydrophobic amino acids, including isoleucine (Ile), leucine (Leu), phenylalanine (Phe), and tryptophan (Trp). Deprivation of these amino acids can induce Ubr1 auto-inhibition.[24] Interestingly, their levels remained largely unchanged under oxidative stress (Figure S2H). This finding prompted us to investigate whether oxidative stress impaired the amino-acid-binding capacity of Ubr1.

We thus performed pull-down assays using Leu-immobilized beads to capture overexpressed FLAG-Ubr1 proteins from S2 cell lysates. To minimize interference from intracellular amino acids, S2 cells were pre-incubated in Krebs-Ringer bicarbonate (KRB) buffer, a minimum nutrient solution. Leu pull-down assays showed substantially reduced Ubr1 binding after H_2O_2 or tBH treatment (Figure S2I), suggesting that oxidative stress likely diminishes the amino-acid-binding ability of Ubr1.

To quantitatively determine Ubr1's amino-acid-binding ability, we purified *Drosophila* Ubr1 protein expressed in HEK293S cells and performed *in vitro* microscale thermophoresis (MST) assay. Under normoxia, Ubr1 bound Leu and Ile with a dissociation constant (K_D) of approximately 30 μM (Figures 1K and S2J), comparable to canonical amino acid sensors like Sestrin2 (K_D of approximately 20 μM) and cytosolic arginine sensor for mTORC1 subunit 1 (CASTOR1) (K_D of approximately 30 μM)[30,31]; however, its binding affinity decreased by approximately 30-fold under oxidative stress (Figures 1K and S2J). Similar reduction was observed for other Ubr1-activating amino acids (Figure S2J). These results conclusively demonstrate that oxidative stress leads to reduced amino-acid-binding ability of Ubr1.

Does the reduced amino-acid-binding capacity of Ubr1 under oxidative stress lead to a corresponding decline in its E3 ligase activity? To test this, we measured the ability of Ubr1 to recognize its substrate Plin2 in S2 cells. Under normoxia, exogenous addition of 100 μM Leu, a physiological concentration,[32] activated Ubr1-Plin2 binding (Figure S2K), and this effect was abolished by H_2O_2, despite identical Leu supplementation (Figure S2K). Importantly, these experiments were performed with ice-cold detergent-extracted lysates from amino-acid-depleted S2 cells, ensuring no fluctuations in endogenous amino acid levels.

The ATPase Hsc70-4 maintains the amino-acid-binding capacity of Ubr1

To elucidate how oxidative stress impairs Ubr1's amino-acid-binding capacity, we performed two co-immunoprecipitation (coIP) experiments coupled with mass spectrometry (MS) to identify Ubr1 interactors. The first immunoprecipitated endogenous Ubr1 in *Drosophila* larval brain lysates, while the second pulled down overexpressed FLAG-Ubr1 in S2 cell lysates (Figure 2A). We identified 73 shared candidate Ubr1-interactors (Tables S1 and S2) and prioritized 11 proteins with more than 5-fold enrichment in the peptide-spectrum matches (PSMs) in Ubr1 immunoprecipitates over immunoglobulin G (IgG) controls. These candidates were then subjected to a small interfering RNA (siRNA) screen (Table S3), using the interaction between Ubr1 and Plin2 as a functional readout.

Hsc70-4, the most abundant member of the heat shock protein (Hsp70) superfamily in both S2 cells and larval brains (Figure S3A),[33,34] was identified as a key regulator of Ubr1 activity (Figures S4A and S4B). Specifically, *Hsc70-4* knockdown in S2 cells abolished the ability of 100 μM Leu to activate Ubr1 (Figure 2B), disrupted Ubr1-Plin2 binding (Figures 2C and S3B), and blocked Plin2 ubiquitination under normoxia (Figures 2D and S3B). As a control, silencing *Hsc70-3* (Figure S3B), another highly expressed member of Hsp70 superfamily (Figure S3A), had no effects (Figures 2C and 2D). CoIP analysis confirmed Hsc70-4-Ubr1 interaction (Figure S3C), further supporting Hsc70-4's role in maintaining Ubr1 function.

To directly assess the impact of Hsc70-4 on Ubr1's amino-acid-binding ability, we performed *in vitro* MST assays. *Drosophila* Ubr1 protein was purified from HEK293S cells either untreated or pretreated with quercetin (Figure S5C), which inhibits the expression of *HSP70* family genes by abrogating DNA-binding of heat shock transcription factors (HSFs) (Figure S5D).[35,36] Ubr1 purified from quercetin-treated HEK293S cells exhibited significantly decreased amino-acid-binding ability, with K_D values increasing approximately

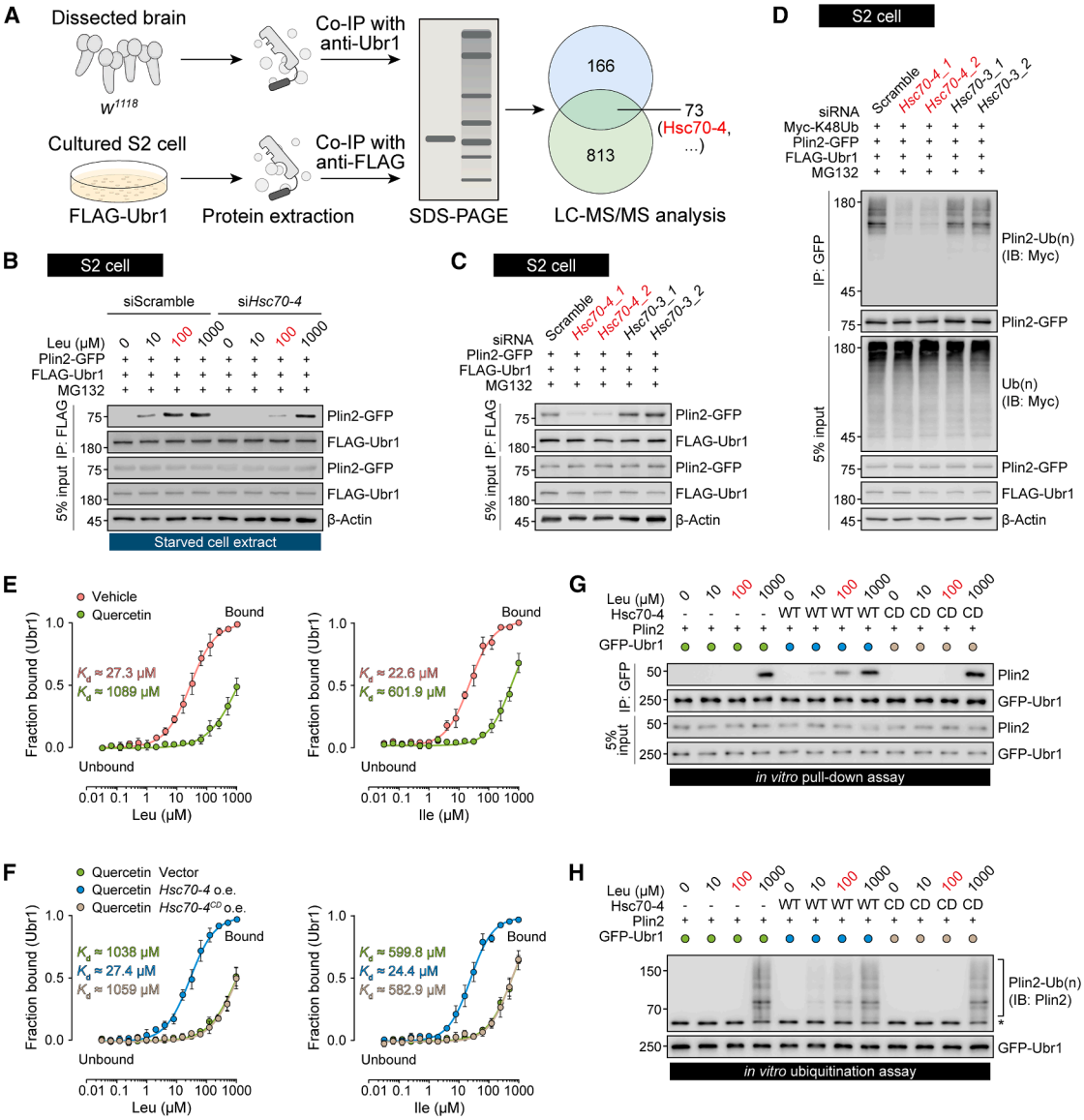

Figure 2. Hsc70-4 regulates amino-acid-induced Ubr1 activity

(A) The schematic depicts two independent coIP tandem MS experiments to identify candidate interactors of Ubr1. 73 candidate interactors common to both experiments were identified. The top 11 candidates were then validated for their function in regulating Ubr1 activity via siRNA screening. Hsc70-4 emerged as a regulator of Ubr1 activity (see also Figures S4A and S4B).

(B) Leu at the indicated concentrations was added to ice-cold detergent-extracted lysates of *Drosophila* S2 cells transfected with control siRNA (siScramble) or *Hsc70-4* targeting siRNA (si*Hsc70-4*). The interaction between FLAG-Ubr1 and Plin2-GFP was assessed. Note that cells were pretreated with 20 μM MG132 for 6 h before harvest to inhibit Plin2-GFP degradation and incubated in nutrient-deprived KRB buffer for 1 h before harvest to deplete intracellular amino acids.

(C) The interaction between FLAG-Ubr1 and Plin2-GFP in S2 cells transfected with control siRNA (siScramble) or siRNAs targeting *Hsc70-4* (si*Hsc70-4*_1 and _2) or *Hsc70-3* (si*Hsc70-3*_1 and _2).

(D) K48-linked ubiquitination levels of Plin2-GFP in S2 cells transfected with siRNAs as described in (C). To prevent Plin2-GFP degradation, 20 μM MG132 was added to the culture medium. The Myc-K48Ub construct contains mutations converting all lysine residues to Arg except for Lys48.

(E and F) The binding affinity of Leu and Ile to GFP-Ubr1 proteins was measured using *in vitro* MST assays (see also Figures S5A and S5B). GFP-Ubr1 proteins used in (E) were purified from HEK293S cells cultured in medium containing 10 μM quercetin or left untreated. For the purification of GFP-Ubr1 proteins used in (F), HEK293S cells transfected with GFP-Ubr1 were co-transfected with an empty vector, wild-type *Hsc70-4*, or the catalytically inactive mutant *Hsc70-4*^{CD}. The transfected cells were then cultured in medium containing 10 μM quercetin. Three biologically independent repeats.

(G) *In vitro* pull-down assays were conducted to assess the interaction between Plin2 and the purified GFP-Ubr1 proteins used in (F) in a cell-free system. Leu was added to the assay at the indicated concentrations.

(H) Plin2 was incubated with ubiquitin, E1 ubiquitin-activating enzyme UBE1, E2 ubiquitin-conjugating enzyme HR2B, and purified GFP-Ubr1 proteins used in (F) in a cell-free system. Leu was added to the reaction at the indicated concentrations. The asterisk denotes unmodified Plin2 protein.

30-fold, as compared with untreated controls (Figures 2E and S5A). This impairment correlated with diminished Plin2 recognition and ubiquitination by Ubr1 in an *in vitro* cell-free system supplemented with physiological concentrations of Leu (Figures 2G and 2H).

Quercetin had no effects on the enzymatic activity of Hsc70-4 *in vitro* (Figure S5E). We therefore hypothesized that reintroduction of Hsc70-4 could reverse quercetin-induced defects. Indeed, wild-type *Hsc70-4* overexpression in HEK293S cells restored the amino-acid-binding ability of purified Ubr1 (Figures 2F and S5B), as well as its ability to bind and ubiquitylate Plin2 (Figures 2G and 2H). As control, the catalytically inactive *Hsc70-4*^{CD} variant, which lacks ATP-binding ability,[37] had no effects (Figures 2F–2H and S5B). These results demonstrate that Hsc70-4 maintains Ubr1's amino-acid-binding ability in an ATPase-dependent manner. Notably, 1,000 μM Leu, approximately 10 times the physiological concentration, restored the activity of Ubr1 purified from quercetin-treated HEK293S cells (Figures 2G and 2H), consistent with residual Leu binding at this concentration observed in MST experiments (Figure 2E).

To examine the physiological significance of this regulation, we analyzed LD accumulation in *Drosophila* larval brains. Glial-specific knockdown of *Hsc70-4*, but not *Hsc70-3*, induced a significant increase in LD contents (Figures S3D–S3G). This phenotype was recapitulated by overexpressing a dominant-negative *Hsc70-4*^{CD} mutant (Figures S3D and S3E), which lacks catalytic activity but can bind Ubr1 (Figure S3H).[37] Importantly, LD accumulation induced by *Hsc70-4* knockdown was rescued by three independent interventions: glial-specific *Plin2* knockdown, overexpression of a constitutively active *Ubr1* (*Ubr1*^{CA}) variant, and introduction of an *Ubr1*^{CA} knockin allele (Figures S3D, S3E, S3I, and S3J). Together, these complementary genetic approaches demonstrate that Hsc70-4 restrains glial LD accumulation by maintaining the activity of Ubr1 to degrade Plin2.

Oxidative stress impairs Hsc70-4 activity via site-specific 4-HNE modification

While oxidative stress did not alter the mRNA or protein level of Hsc70-4 (Figures S6A and S6B), it reduced Hsc70-4's ATP-binding capacity (Figure 3A) and ATPase activity (Figure 3B) when exogenously expressed. These observations led us to investigate whether oxidative stress triggered post-translational modifications that regulate Hsc70-4 function.

We performed electron-transfer/higher-energy collision dissociation-MS (EThcD-MS) on Hsc70-4. A covalent 4-HNE modification was detected on Cys267 in Hsc70-4 isolated from extracts of larval brains exposed to hypoxia (Figure 3C). This modification is consistent with modest upregulation of 4-HNE levels during oxidative stress (Figures 1D and 1E) and 4-HNE's known propensity to non-enzymatically modify redox-sensitive proteins at cysteine residues, using a carbon-carbon double bond.[27] To identify the specificity of this modification, we reconstituted this HNEylation reaction *in vitro* (Figure 3D) using recombinant *Drosophila* Hsc70-4 proteins (Figure S5C). Wild-type Hsc70-4, but not the Hsc70-4^{C267A} mutant, underwent 4-HNE adduction (Figure 3E), confirming Cys267 as the specific site of 4-HNE adduct formation. Importantly, 4-HNE-modified Hsc70-4 exhibited impaired ATP-binding capability (Figure 3E) and ATPase activity (Figure 3F), mirroring oxidative stress-induced defects. Consistently, structural modeling positioned Cys267 adjacent to the Hsc70-4's ATPase domain (Figure 3C), suggesting that 4-HNE adduction may induce steric hindrance that disrupts ATP binding.

We next asked whether 4-HNE-mediated Hsc70-4 inactivation compromised Ubr1 activity in Plin2 degradation. MST assays revealed that Ubr1 proteins, purified from HEK293S cells treated with 4-HNE, exhibited diminished amino-acid-binding capacity as compared with untreated controls (Figures 4A and S6C). Accordingly, *in vitro* assays showed that 100 μM Leu failed to activate Ubr1—purified from 4-HNE-treated HEK293S cells—to recognize and ubiquitylate Plin2 (Figures 4B and 4C). This regulatory mechanism is physiologically relevant in S2 cells and larval brains. 4-HNE treatment attenuated the interaction between Plin2 and Ubr1 (Figure 4D), while *ex vivo* 4-HNE exposure induced glial LD accumulation in normoxic larval brains (Figures S6D and S6E). Notably, these effects were abolished in S2 cells expressing the constitutively active Ubr1^{CA} variant, which maintained the ability to bind to Plin2 even in the presence of 4-HNE (Figure 4E), and in *Ubr1*^{CA} knockin flies, which are resistant to 4-HNE-induced glial LD accumulation (Figures S6D and S6E).

Blocking 4-HNE modification of Hsc70-4 prevents oxidative stress-induced glial LD accumulation

Given the critical role of the 4-HNE modification in impairing Hsc70-4 activity and Ubr1 function, we hypothesized that blocking this modification would restore Ubr1 function and prevent glial LD accumulation even in the presence of 4-HNE. Indeed, MST analysis suggested that overexpressing 4-HNE modification-resistant *Hsc70-4*^{C267A}, but not wild-type *Hsc70-4*, in HEK293S cells reversed the inhibitory effect of 4-HNE on the amino-acid-binding ability of purified Ubr1 (Figures 4F and S6C). This restoration enabled 100 μM Leu to activate Ubr1—purified from 4-HNE-treated HEK293S cells—to recognize and ubiquitylate Plin2 *in vitro* (Figures 4B and 4C).

To validate these findings *in vivo*, we generated *Hsc70-4*^{C267A} knockin flies. In homozygotic *Hsc70-4*$^{C267A/C267A}$ larval brains, 4-HNE-induced glial LD accumulation was blocked (Figures 4G and 4H). Furthermore, *Hsc70-4*$^{C267A/C267A}$ larvae resisted oxidative stress-induced glial LD accumulation (Figures 5A and S6G), leading to elevations in 4-HNE and ROS levels (Figures 5B, 5C, and S6F). Importantly, these phenotypes were reversed by genetic elimination of *Ubr1* (Figures 5A–5C, S6F, and S6G). To assess cell-type-specific effects, we overexpressed *Hsc70-4*^{C267A} specifically in glial cells. This intervention suppressed LD accumulation under oxidative stress (Figures S6H and S6I), while elevating 4-HNE and ROS levels in larval brains (Figures S6J–S6L), phenocopying findings in *Hsc70-4*$^{C267A/C267A}$ flies. Together, these results define a cascade wherein oxidative stress induces 4-HNE modification of Hsc70-4 at Cys267, inactivating its ATPase activity. This impairs Ubr1's activity to degrade Plin2, leading to glial LD accumulation as a compensatory antioxidant mechanism. Blocking 4-HNE modification restores Hsc70-4's ability to promote Ubr1-mediated Plin2 degradation, thereby disrupting LD-dependent redox homeostasis (Figure 5G).

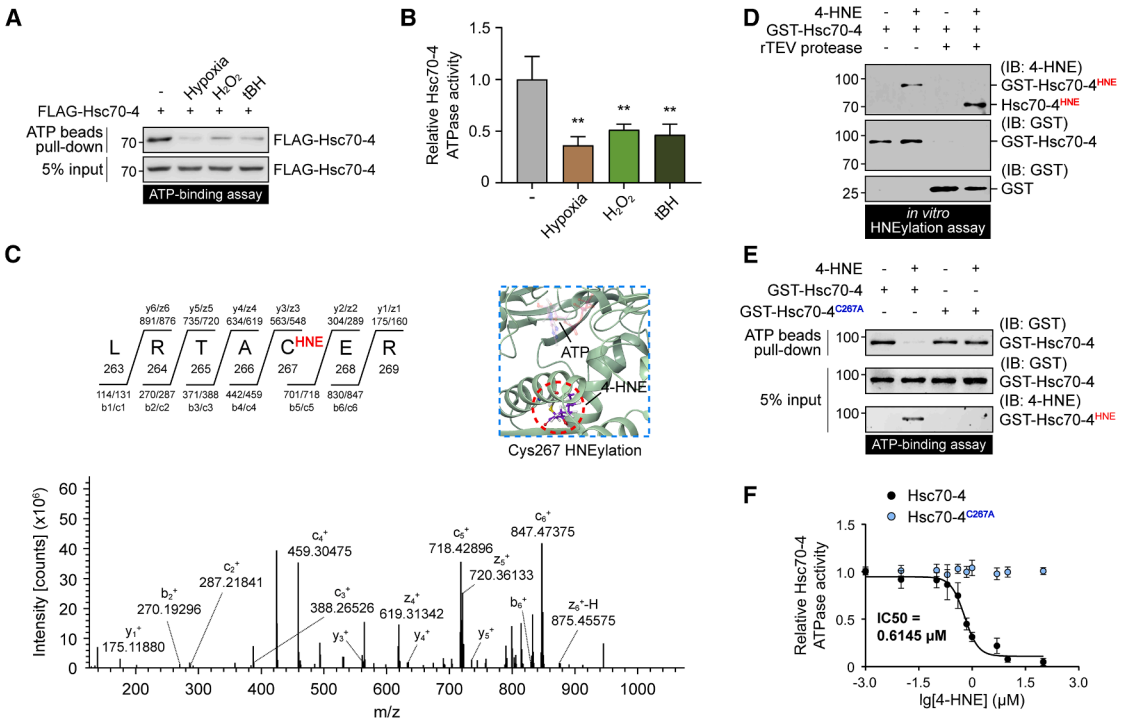

Figure 3. 4-HNE covalently modifies and inactivates Hsc70-4 during oxidative stress

(A) FLAG-Hsc70-4 proteins purified from *Drosophila* S2 cells were pulled down using ATP-immobilized beads. Cells were exposed to 16-h normoxia or hypoxia or 1-h treatments of 200 μM H_2O_2 or 200 μM tBH before harvest.

(B) ATPase activity of the purified FLAG-Hsc70-4 proteins described in (A) was quantified via a colorimetric assay. Three independent experiments. One-way ANOVA, Dunnett's multiple comparison tests.

(C) MS spectra of the peptide from endogenous Hsc70-4 protein purified from *Drosophila* larval brains after 16-h hypoxia. A 4-HNE modification was identified on Cys residue at position 267 of Hsc70-4 (peptide precursor ion mass: 502.7828 [2+], mass error: 2.6 ppm, Xcorr (score): 3.39). Fragment ions (b/c: N-terminal; y/z: C-terminal) are annotated. A predictive structural model of 4-HNE-modified Hsc70-4 is shown for comparison.

(D) *In vitro* HNEylation assays identified 4-HNE modification on glutathione S-transferase (GST)-Hsc70-4 protein, purified from bacteria, after addition of 1 mM 4-HNE to the system. This modification remained detectable on Hsc70-4 after GST tag removal using recombinant tobacco etch virus (rTEV) protease. Note that blots for GST-Hsc70-4^{HNE} and GST-Hsc70-4 were stripped and re-blotted on the same membrane.

(E) ATP-immobilized beads were used to pull down wild-type GST-Hsc70-4 or the GST-Hsc70-4^{C267A} mutant proteins purified from bacteria. Proteins were pretreated with 1 mM 4-HNE or left untreated for 1 h. Note that blots for GST-Hsc70-4^{HNE} and GST-Hsc70-4 in the input group were stripped and re-blotted on the same membrane.

(F) ATPase activity of purified wild-type GST-Hsc70-4 and GST-Hsc70-4^{C267A} mutant proteins, pretreated with indicated concentrations of 4-HNE for 1 h, was measured using a colorimetric assay. The half maximal inhibitory concentration (IC_{50}) is shown. Three independent experiments.

The regulation of Hsc70-4 on Ubr1 activity is evolutionarily conserved

In previous experiments, we observed a significant reduction in the amino-acid-binding capacity of *Drosophila* Ubr1 purified from mammalian HEK293S cells treated with quercetin to suppress expression of *HSP70* family genes (Figures 2E and S5A). This reduction suggested that the regulation of Hsc70-4 on Ubr1 activity may be evolutionarily conserved. We thus examined HSPA8, the human ortholog of *Drosophila* Hsc70-4.[38] CoIP experiments performed in human oligodendrocyte-like MO3.13 cells showed that endogenous HSPA8 interacted with both UBR1 and UBR2 (abbreviated as UBR1/2) (Figure S7A), the human orthologs of *Drosophila* Ubr1,[24] mirroring the Hsc70-4-Ubr1 interaction in fly S2 cells (Figure S3C). Consistent with our findings in fly cells, knocking down *HSPA8* in MO3.13 cells prevented UBR1/2 from recognizing perilipin 2 (PLIN2) (Figures S7B and S7C). By contrast, silencing other abundant members of HSP70 family proteins had no effects (Figures S7B–S7D), highlighting the specificity of HSPA8 in this regulation.

Cys 267, targeted by 4-HNE in *Drosophila* Hsc70-4, is conserved in mammalian HSPA8 (Figure S7G). Does 4-HNE modification also regulate HSPA8 in mammals? *In vitro* HNEylation assays using recombinant mouse and human HSPA8 proteins, both purified from bacteria (Figure S7H), confirmed robust 4-HNE adduction at Cys267 (Figures S7E and S7F). Mutation of Cys267 to Ala completely abolished the 4-HNE modification (Figures S7E and S7F), demonstrating site specificity. We next asked whether 4-HNE modification of HSPA8 under oxidative stress also induced LD accumulation in mammalian systems. Indeed, treatment with H_2O_2 increased LD numbers in human MO3.13 cells (Figures 5D and 5E). This was reversed by overexpression of *HSPA8*^{C267A} (Figures 5D and 5E) and subsequently led to a significant elevation in ROS levels, as demonstrated by

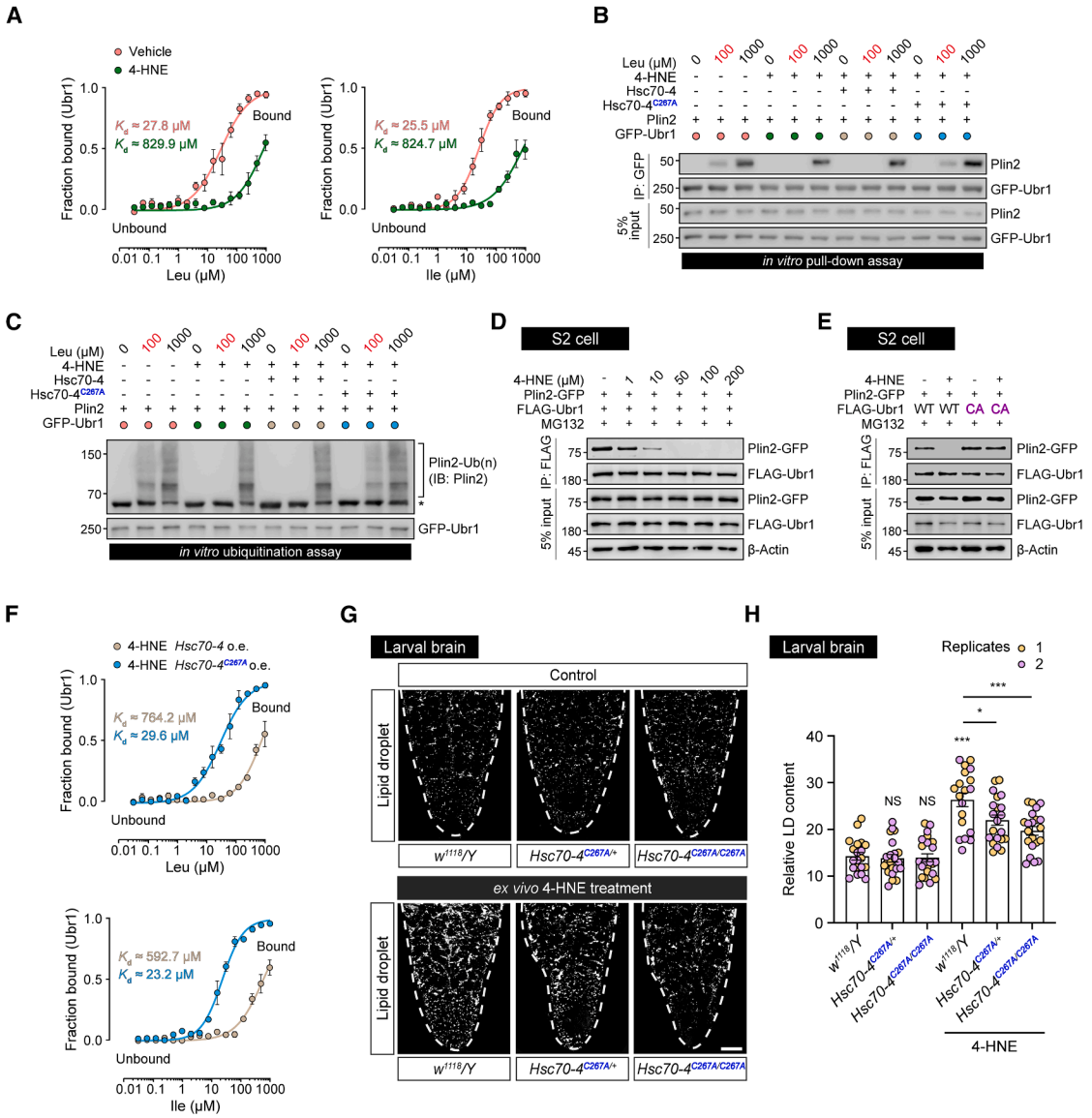

Figure 4. Hsc70-4^{C267A} restores the amino-acid-induced Ubr1 activity in the presence of 4-HNE

(A) *In vitro* MST assays were used to quantify the binding affinity of Leu and Ile to GFP-Ubr1 proteins purified from HEK293S cells (see also Figure S6C). HEK293S cells were treated with 10 μM 4-HNE or left untreated for 1 h before harvest. Three biologically independent repeats.

(B) *In vitro* pull-down assays were performed to assess the interaction between Plin2 and purified GFP-Ubr1 proteins used in (A) and (F) in a cell-free system. Leu was added to the reaction at the indicated concentrations.

(C) Plin2 was incubated with ubiquitin, E1 ubiquitin-activating enzyme UBE1, E2 ubiquitin-conjugating enzyme HR2B, and purified GFP-Ubr1 proteins used in (A) and (F) in a cell-free system. Leu was added to the reaction at the indicated concentrations. The asterisk denotes unmodified Plin2 protein.

(D) The interaction between wild-type FLAG-Ubr1 and Plin2-GFP in S2 cells treated with 4-HNE of the indicated concentrations for 1 h.

(E) The interaction of the wild-type and constitutively activated FLAG-Ubr1 with Plin2-GFP in S2 cells exposed to medium containing 100 μM 4-HNE or left untreated for 1 h.

(F) *In vitro* MST assays were used to quantify the binding affinity of Leu and Ile to GFP-Ubr1 proteins purified from HEK293S cells (see also Figure S6C). HEK293S cells were co-transfected with wild-type *Hsc70-4* or *Hsc70-4*^{C267A} mutant and treated with 10 μM 4-HNE for 1 h before harvest. Three biologically independent repeats.

(G and H) LDs (white, BODIPY-stained) in the brains of *Drosophila* late-third instar larvae of different genotypes (*Hsc70-4*$^{C267A/+}$, *Hsc70-4*$^{C267A/C267A}$, control: *w*^{1118}/*Y*) (G). Larval brains were treated with 100 μM 4-HNE or left untreated for 1 h before fixation. Quantification of relative LD content is shown in (H). *n* = 19–23 larval brains from two independent experiments. One-way ANOVA, Tukey's multiple comparison tests. Scale bar, 50 μm.

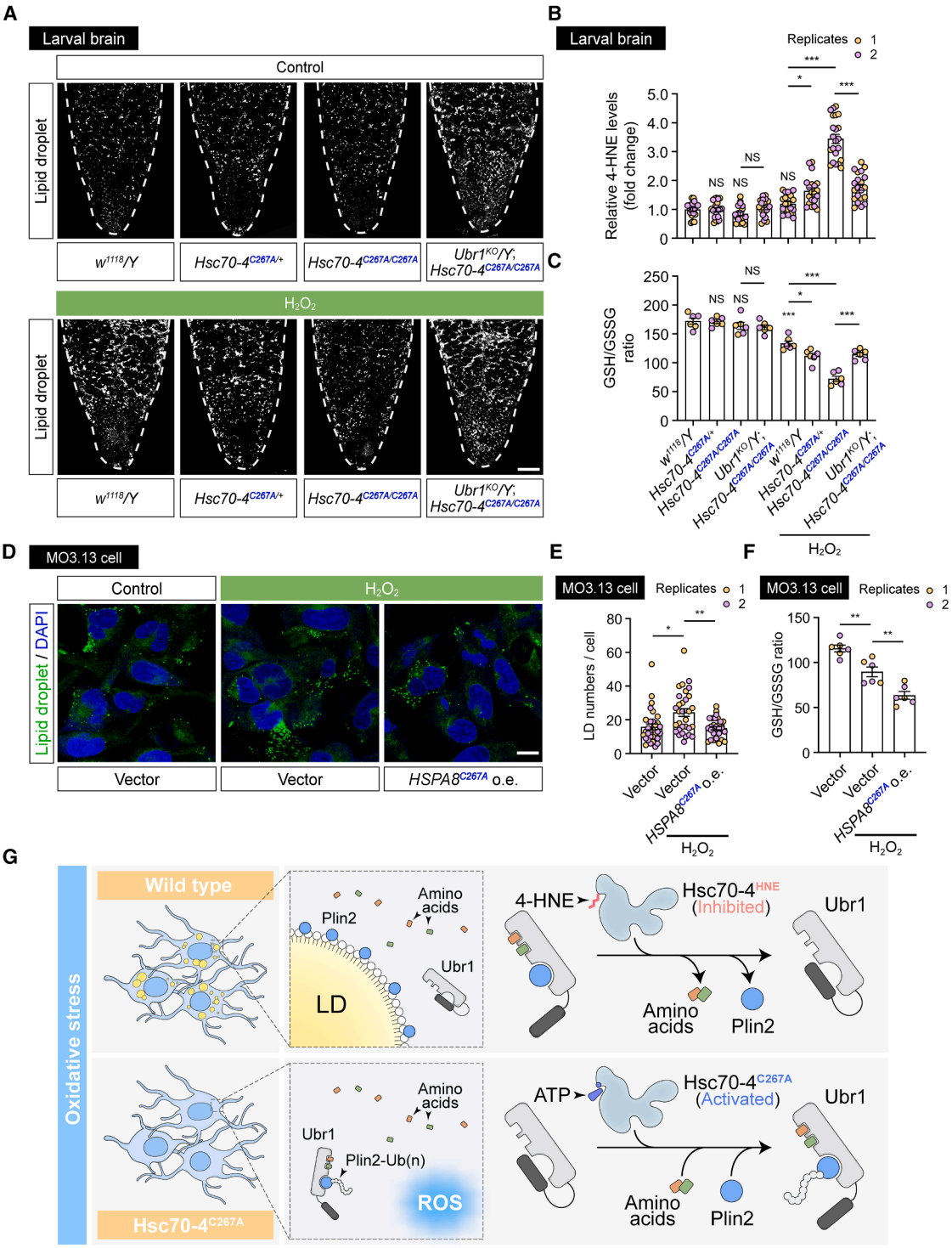

Figure 5. 4-HNE modification of Hsc70-4 as an evolutionarily conserved, LD-dependent mechanism against oxidative stress

(A–C) LDs (white, BODIPY-stained) (A), 4-HNE adduct levels (B), and GSH/GSSG ratios (C) in the brains of *Drosophila* late-third instar larvae of different genotypes (*Hsc70-4*$^{C267A/+}$, *Hsc70-4*$^{C267A/C267A}$, *Ubr1*^{KO}/*Y*; *Hsc70-4*$^{C267A/C267A}$, control: w^{1118}/*Y*). Larvae were exposed to 16-h H_2O_2 treatment or left untreated before harvest. In (B), n = 19–22 larval brains from two independent experiments. In (C), n = 6 biological samples (each containing 20 larval brains) from two independent experiments. One-way ANOVA, Tukey's multiple comparison tests. Scale bar, 50 μm.

(D–F) LDs (green, BODIPY-stained) (D), quantification of average LD numbers per cell (E), and GSH/GSSG ratios (F) in oligodendrocyte-like human MO3.13 cells transfected with *HSPA8*^{C267A} or empty vector. Cells were treated with 250 μM H_2O_2 or left untreated for 1 h before harvest. In (E), n = 31 frame views of cells

(legend continued on next page)

a reduced GSH/GSSG ratio (Figure 5F). Together, these findings reveal an evolutionarily conserved mechanism wherein lipid peroxidation-derived 4-HNE modification of HSPA8 prevents amino acids from activating UBR1/2-mediated PLIN2 degradation under oxidative stress. This defect promotes glial LD accumulation, which protects unsaturated lipids against ROS attack (Figure 5G).

Enhancing HSPA8 activity as a therapeutic strategy for glioma treatment

Glioma, the most prevalent and aggressive form of brain cancer, is characterized by rapid growth, extensive invasion, and high recurrence rates. These features are particularly pronounced in grade 4 GBM, the most lethal subtype of glioma.[39–41] Despite therapeutic advances, the median survival of GBM patients is only 14.5–16.6 months post diagnosis.[42] Glioma cells have been shown to evade ROS-induced death by exploiting LD-dependent antioxidant mechanisms, wherein LDs sequester peroxidation-prone unsaturated lipids.[20–22] Our analyses of The Cancer Genome Atlas (TCGA) showed that elevated expression of *PLIN2* correlates with poor prognosis in glioma patients (Figure 6A), providing human genetic evidence supporting this model. We validated this finding in 18 tumor specimens from glioma patients (Figure 6B), showing a positive correlation between PLIN2 protein level and tumor malignancy grade (Figure 6C).

To investigate the molecular basis of PLIN2 upregulation, we assayed 4-HNE modification on HSPA8 in these specimens (Figure 6B). 4-HNE modification level of HSPA8 was markedly elevated in high-grade glioma, correlating with poor prognosis in glioma patients (Figures 6D and 6E). Importantly, PLIN2 level positively associated with the extent of 4-HNE modification of HSPA8 (Figure 6F), consistent with our earlier finding that 4-HNE modification of HSPA8 stabilized PLIN2 (Figure 5G). These observations prompted us to hypothesize that enhancing HSPA8 activity by blocking its 4-HNE modification would destabilize PLIN2, disrupt antioxidative LD reservoirs, and trigger ROS-mediated glioma cell death.

We overexpressed *HSPA8*^{C267A}, a 4-HNE modification-resistant HSPA8 variant (Figure S7F), in human U87MG, U251MG, and T98G glioma cells. This intervention markedly reduced PLIN2 protein levels (Figures S8A–S8C) and significantly elevated ROS levels, as evidenced by decreased GSH/GSSH ratios (Figures S8D–S8F). Thus, *HSPA8*^{C267A} overexpression suppressed tumor cell growth (Figures S8G–S8I) and induced apoptosis, marked by caspase-3 cleavage (Figures S8A–S8C). Importantly, these effects were reversed by the ROS scavenger N-acetyl-cysteine (NAC) (Figures S8D–S8I), confirming that *HSPA8*^{C267A}-mediated tumor cell growth attenuation and apoptosis are ROS-dependent.

We next evaluated the therapeutic potential of this strategy in orthotopic glioma models. Athymic nude mice brains implanted with *HSPA8*^{C267A}-expressing U87 cells exhibited substantially reduced tumor size and growth (Figures 7A and 7C), as compared with the control group. The overall survival of mice with grafted tumors was extended from an average of about 20 to 50 days (Figure 7D). Tumors showed diminished PLIN2 protein levels (Figure 7B), reduced LD contents (Figures 7A and 7E), and elevated ROS levels (Figure 7F), accompanied by activated caspase-3 cleavage and apoptotic cell death (Figures 7A and 7G). To confirm that these anti-glioma effects were due to the enhanced amino-acid-binding ability of UBR1/2, we employed Leu-immobilized beads to pull down endogenous UBR1/2 from the lysates of U87 cells, deprived of intracellular amino acids before harvest. As predicted, *HSPA8*^{C267A} overexpression in U87 cells increased recruitment of UBR1/2 by Leu-immobilized beads (Figure 7H), consistent with restored amino-acid-binding ability. Replications in a GL261 cell-derived orthograft glioma mouse model yielded concordant anti-tumor effects (Figures S8J–S8L). Taken together, our results establish a critical knowledge bridge by elucidating how oxidative stress drives glial LD accumulation. Moreover, by demonstrating that 4-HNE modification of HSPA8 stabilizes PLIN2 to sustain antioxidant defense, we identify HSPA8 activation as a potential therapeutic strategy for glioma treatment.

DISCUSSION

Cellular adaptation to environmental fluctuations, particularly oxidative stress and excessive ROS production, is essential for maintaining cellular integrity and for organismal survival. To counteract these challenges, cells evolved diverse strategies, including the activation of antioxidant transcription factors and upregulation of protective metabolites.[1–4] Here, we identify an integrated antioxidant sensing and regulatory mechanism, which coordinates amino-acid-sensing pathways, antioxidant responses, and dynamic regulation of LDs.

Amino acid sensing is central to cellular adaptation, enabling organisms to adjust to nutrient fluctuations in extracellular and intracellular microenvironments. Previous studies identified sensors with fixed, amino-acid-specific binding affinities. For instance, Sestrin2 binds Leu with a K_D of approximately 20 μM, allowing Leu detection in nutrient-rich contexts, such as adipocytes,[31,43] and this interaction modulates the activity of the mammalian target of rapamycin (mTOR) complex 1 (mTORC1), thereby regulating cell growth. The alternative Leu sensor SAR1B, by contrast, has a higher Leu-binding affinity, with a K_D of about 2 μM, sustaining mTORC1 activity even under Leu-limited conditions, as in protein synthesis-active myotubes.[43] Our study reveals an alternative strategy of sensor affinity regulation by small molecule binding: covalent modification of the ATPase Hsc70-4 by 4-HNE dynamically tunes the amino-acid-binding affinity of Ubr1, an amino-acid-activated E3 ligase. This plasticity enables cells to sense amino acid fluctuations using a single sensor. Given that canonical sensors, such as

(dimensions 60 × 60 μm) from two independent experiments. In (F), n = 6 biological samples from two independent experiments. One-way ANOVA, Tukey's multiple comparison tests. Scale bar, 10 μm.

(G) Schematic model of an evolutionarily conserved mechanism for glial cells accumulating LDs to counteract oxidative stress. Under oxidative stress, 4-HNE inhibits the ATPase activity of Hsc70-4, rendering Ubr1 resistant to amino-acid-induced activation. This stabilizes Plin2, enabling LD accumulation in glial cells as a protective antioxidant response. Reactivation of Hsc70-4 disrupts this LD-dependent antioxidant mechanism, elevating ROS levels and lipid peroxidation.

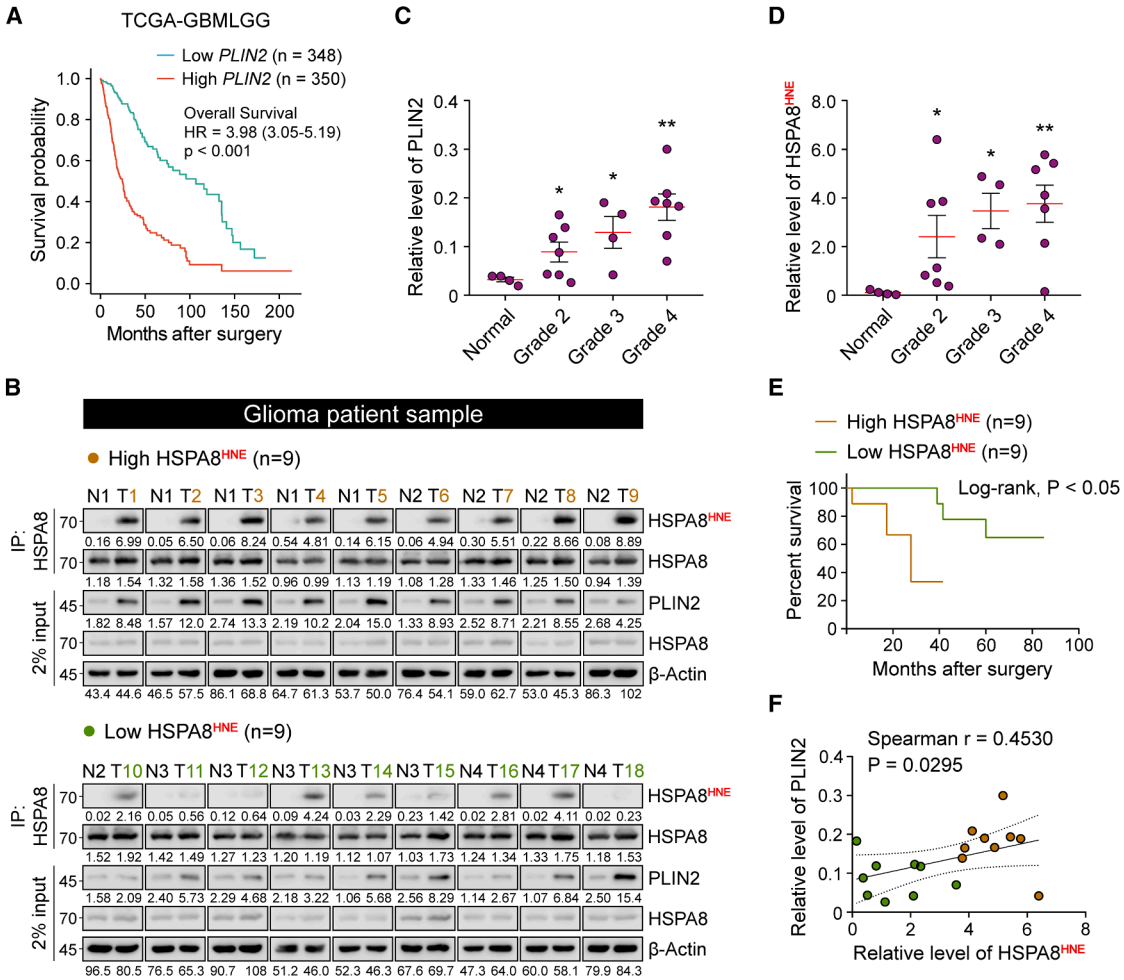

Figure 6. Modification of HSPA8 by 4-HNE correlates with a poor prognosis in glioma patients

(A) Kaplan-Meier survival plot for glioma patients based on *PLIN2* mRNA expression from the TCGA dataset. *p* value was calculated using the log-rank test. GBMLGG, glioblastoma and lower-grade glioma.

(B) Levels of 4-HNE modified HSPA8 and PLIN2 protein expression in normal brain tissues (N) versus glioma tumor samples (T). Eighteen glioma tumor samples (each from an individual patient) with corresponding tumor grades and survival data were categorized into high (top 50%, $n = 9$ samples) and low (bottom 50%, $n = 9$ samples) $HSPA8^{HNE}$ groups based on the $HSPA8^{HNE}$/HSPA8 immunoblot pixel intensity ratio. Note that blots for $HSPA8^{HNE}$ and HSPA8 in the IP group were stripped and re-blotted on the same membrane.

(C and D) PLIN2 levels (C) and 4-HNE modification of HSPA8 (D) in normal brain tissues and glioma tumor samples stratified by tumor grades. PLIN2 levels were quantified as the PLIN2/β-actin immunoblot pixel intensity ratio, and 4-HNE modification of HSPA8 was calculated as the $HSPA8^{HNE}$/HSPA8 ratio shown in (B). $n = 4$–7 samples, one sample per patient. Note that each data point in the "normal" group represents the mean of technical replicates shown in (B). One-way ANOVA, followed by Dunnett's multiple comparison tests.

(E) Kaplan-Meier survival analysis for glioma patients based on levels of 4-HNE modification of HSPA8 in tumor tissues (based on $HSPA8^{HNE}$/HSPA8 ratios from B). *p* value was calculated using the log-rank test.

(F) Spearman's rank correlation analysis between levels of 4-HNE modification of HSPA8 ($HSPA8^{HNE}$/HSPA8 ratio shown in B) and PLIN2 expression (PLIN2/β-actin shown in B) in glioma tumor samples. $n = 18$ samples, one sample per patient.

CASTOR and Sestrins, have not been reported to have this adaptability,[30,31,43] we propose that Hsc70-4 family proteins and/or associated regulatory factors may function as general sensor regulators to fine-tune sensor activity in response to tissue-specific metabolic demands.

In addition to metabolic adaptation, this dynamic amino-acid-sensing mechanism likely also serves as an antioxidant strategy. Lipid peroxidation-derived 4-HNE, which triggers LD-dependent antioxidant response, impairs Hsc70-4 activity. Importantly, this pathway repurposes 4-HNE adducts, traditionally viewed as passive markers of ferroptosis—an iron-dependent, lipid peroxidation-driven cell death pathway[44–48]—into activators of a stress-adaptive survival pathway. We propose a biphasic model for 4-HNE signaling. During milder oxidative stress, modest levels of 4-HNE are generated, reducing Hsc70-4 activity, which in turn promotes LD accumulation and sequestration of peroxidation-prone lipids, thereby mitigating ROS propagation and providing cellular protection. Under these conditions,

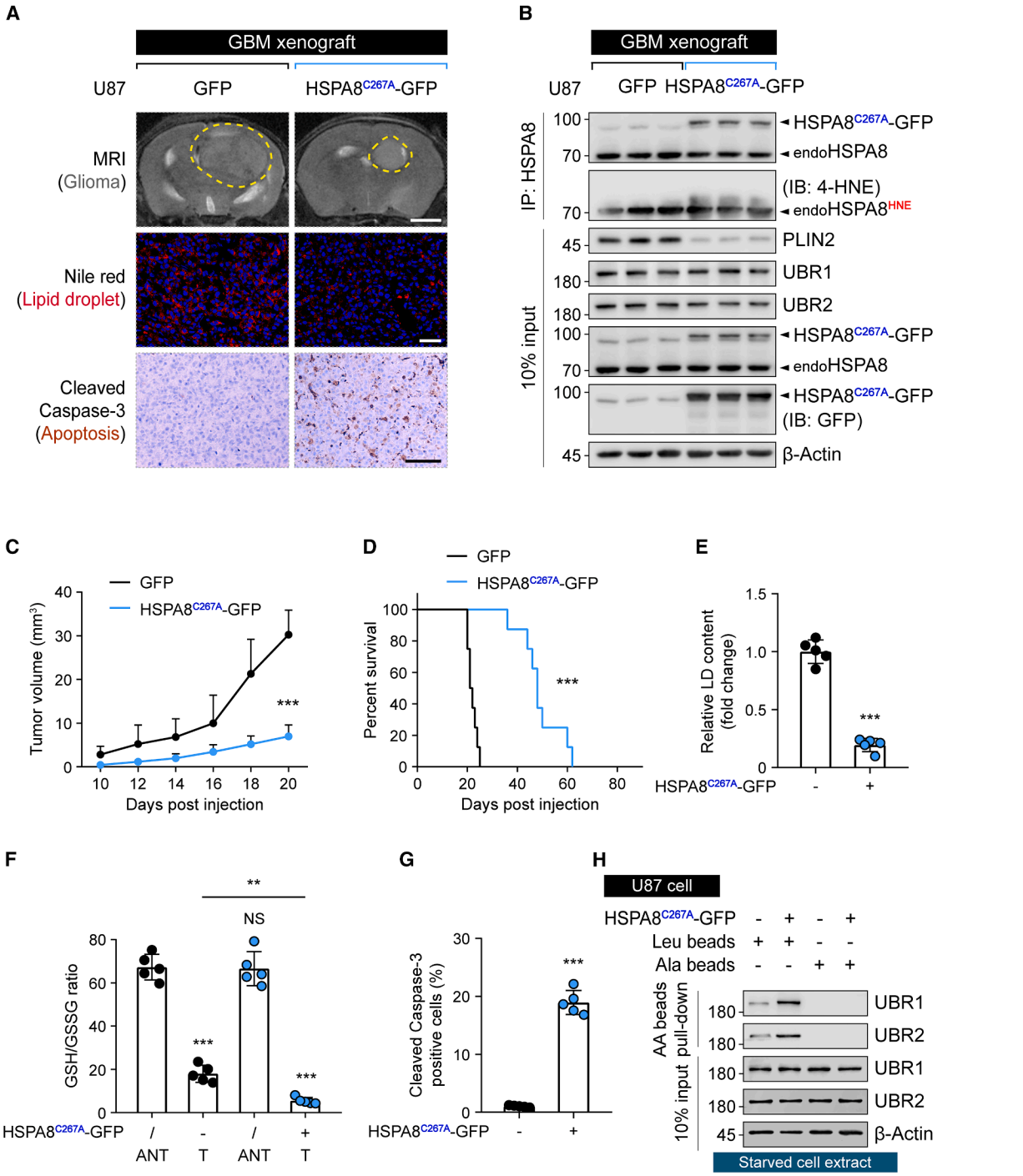

Figure 7. Enhancing HSPA8 activity by expressing *HSPA8*^{C267A} ameliorates glioma

(A) Representative T2-weighted magnetic resonance imaging (MRI) slices of the entire mouse brain and corresponding immunofluorescence (IF) staining for neutral lipids (by Nile red) and immunohistochemistry (IHC) for cleaved caspase-3 (by anti-cleaved caspase-3) in xenograft tumor sections. Mice were intracranially injected with U87 cells stably expressing *GFP* or *HSPA8*^{C267A}*-GFP*, and tissues were collected at day 20 post-injection. Scale bars, 2 mm (MRI), 50 μm (IF), and 80 μm (IHC).

(B) Immunoblot analyses of 4-HNE-modified endogenous HSPA8 protein (endoHSPA8), UBR1/2, and PLIN2 in *GFP* or *HSPA8*^{C267A}*-GFP*-expressing tumors. Note that blots for $_{endo}$HSPA8^{HNE} and $_{endo}$HSPA8 (IP group), UBR1 and UBR2 (input group), and HSPA8^{C267A}-GFP (input group, blotted with HSPA8 and GFP) were, respectively, stripped and re-blotted on the same membrane.

(C) Tumor growth in the mouse brain was quantified by MRI. *n* = 8 mice per group. Multiple t test.

(legend continued on next page)

wild-type flies exhibit only a modest increase in total brain 4-HNE protein adduct level (Figures 1D and 1E). This level of 4-HNE is sufficient to modify Hsc70-4, likely due to the high abundance of Hsc70-4. When 4-HNE modification of Hsc70-4 is blocked, total 4-HNE protein adducts elevate by approximately 3-fold (Figures 5B and S6F). These results highlight the critical role of the LD-dependent antioxidant response under physiological conditions. Under sustained stress conditions, such as exposure to ferroptosis-inducing agents, however, uncontrolled ROS production leads to a burst in 4-HNE adducts, accumulating into systemic overload and ultimately driving cell death. This model integrates 4-HNE's dual functions. The early, targeted modification of Hsc70-4 initiates a protective response, while widespread 4-HNE accumulation drives ferroptotic cell death. Future studies using temporal profiling of 4-HNE protein adducts via high-resolution MS during stress progression will be critical for clarifying these dynamics.

Our study identifies Hsc70-4 as a critical activator of amino-acid-induced Ubr1 activity, in addition to its canonical role as a molecular chaperone facilitating nascent protein folding. Although our *in vitro* findings demonstrate that co-expression of *Hsc70-4* enhances the amino-acid-binding ability of purified Ubr1 proteins (Figures 2E and 2F), enabling activation of Ubr1 and subsequent ubiquitylation of substrate Plin2 (Figure 2H), it is yet unknown whether Hsc70-4 regulates newly synthesized or mature Ubr1. We note that activation of Hsc70-4 by blocking its 4-HNE modification during oxidative stress, a condition in which global translation is suppressed,[2] still enhances amino-acid-induced Ubr1 activity and subsequent LD decomposition. Thus, Hsc70-4 most likely modulates Ubr1 activity independently of its canonical chaperone function in nascent protein folding, pending more definitive structural-functional evidence.

Consistent with their roles in redox regulation, LDs are critical mediators of neuroprotection. During oxidative stress or neuronal hyperactivity, neurons transfer cytotoxic lipid peroxides to neighboring glial cells for detoxification via β-oxidation,[13] elevating glial ROS levels and driving LD accumulation. These glial LDs shield PUFAs from peroxidation and facilitate mitochondrial clearance of oxidized lipids, thus mitigating ROS overproduction and neuronal damage.[11,15] Remarkably, this neuron-glia lipid-handling process is evolutionarily conserved, with LD-mediated antioxidant defenses observed from *Drosophila* to mammals.[15–18] On the other hand, aberrant LD accumulation is also a prevalent feature in diverse malignancies, including lung, liver, clear cell renal cell carcinoma, and brain cancers,[19,21,49–52] suggesting that cancer cells might hijack LD-dependent antioxidant mechanisms to survive oxidative stress. Consistently, in glioma models, expression of the 4-HNE modification-resistant *HSPA8*^{C267A} mutant reduces the LD-stabilizing protein PLIN2 and depletes LD content, effectively disrupting tumor-promoting antioxidant adaptations. Beyond cancer, pathological LD deposition is linked to metabolic dysfunction-associated steatotic liver disease (MASLD) and Alzheimer's disease (AD), where oxidative stress and lipid peroxidation further exacerbate disease pathology.[24,53–55] Therapeutic strategies targeting LD dynamics, such as HSPA8^{C267A}-mediated LD suppression, may thus offer promise for the treatment of these diseases.

The dual role of LDs, protective in neurophysiology and disruptive in disease, highlights the importance of precise regulatory mechanisms. Central to this balance is 4-HNE, which functions as a metabolic rheostat coordinating nutrient sensing, redox balance, and organelle adaptability. By identifying the bridge between amino-acid-sensing flexibility and LD regulation, our study reveals a new mechanism through which cells dynamically respond to metabolic challenges. Therapeutically, disrupting LD dynamics or its sensor plasticity could induce specific tumor vulnerabilities, while modulating LD accumulation may alleviate oxidative damage in pathologies such as neurodegenerative and metabolic diseases.

Limitations of the study

In this study, we showed that Hsc70-4 regulates the amino-acid-binding ability of Ubr1. However, the underlying mechanism remains elusive. Structural and biochemical analyses are needed to determine whether this involves conformational changes in Ubr1, recruitment of auxiliary factors, or other processes. Additionally, while LDs shield PUFAs from peroxidation,[11,12] the underlying mechanism remains unresolved. Future studies would determine whether this is due to ROS inaccessibility or antioxidant co-accumulation to protect these peroxidation-prone lipids. Resolving these gaps is essential for fully understanding how amino acid sensing integrates with stress-responsive, LD-mediated antioxidant pathways and is critical for evaluating HSPA8's potential as a therapeutic target in redox-associated pathologies.

RESOURCE AVAILABILITY

Lead contact

Further information and requests for resources and reagents should be directed to and will be fulfilled by the lead contact, Alan Jian Zhu (zhua@pku.edu.cn).

Materials availability

All the materials generated in this study are available from the lead contact without restriction.

(D) Mouse survival was assessed by Kaplan-Meier curves. $n = 8$ mice per group. Log-rank test.
(E) Relative LD content in xenograft tumor sections shown in (A). $n = 5$ frame views of tumor sections (dimensions 400 × 300 μm), each from an individual mouse. Two-tailed Student's t test.
(F) GSH/GSSG ratios in xenograft tumor tissues (T) versus adjacent normal brain tissues (ANTs) shown in (A). $n = 5$ normal brain tissues or tumor tissues, each from an individual mouse. One-way ANOVA with Tukey's multiple comparison tests.
(G) Percentage of cleaved caspase-3-positive cells in xenograft tumor sections shown in (A). $n = 5$ frame views of tumor sections (dimensions 300 × 225 μm), each from an individual mouse. Two-tailed Student's t test.
(H) The amino-acid-binding affinity of UBR1/2 assessed using Leu-immobilized beads in lysates from starved U87 cells expressing *GFP* or *HSPA8*^{C267A}*-GFP*. Ala-immobilized beads served as a negative control.

Data and code availability

- Original western blot images have been deposited at Mendeley at (DOI: https://doi.org/10.17632/5mrzngzfyh.1) and are publicly available as of the date of publication. Raw microscopy data reported in this paper will be shared by the lead contact upon request.
- This paper does not report original code.
- Any additional information required to reanalyze the data reported in this paper is available from the lead contact upon request.

ACKNOWLEDGMENTS

We thank Drs. Jianguo Chen, Xiaowei Chen, Alex P. Gould, Xun Huang, Zhe Zhang, Joel D. Levine, Yi Li, Anne Plessis, Yi Rao, Ruiping Xiao, Jing Yang, Xiang Yu, and Qiang Zhou; DSHB; VDRC; the Bloomington Drosophila Stock Center; the Tsinghua Fly Center; and the National Institute of Genetics (Kyoto) for fly stocks and reagents. We also thank Drs. Chunyan Shan, Guilan Li, Hongxia Lv, Yonglu Tian, and Jing Tian at the National Center for Protein Science at Peking University for assistance with microscopic imaging, short hairpin RNA (shRNA) library, flow cytometry, and behavioral experiments; Wen Zhou at the Analytical Instrumentation Center of Peking University for help with mass spectrum analyses; and Weijie Bian at the Biomolecular Interaction Analysis Platform and Jian Zhong at the Cell Imaging Platform at Peking University Chengdu Academy for Advanced Interdisciplinary Biotechnologies for technical assistance. This work was supported by the National Natural Science Foundation of China (32330026 to A.J.Z., 32300990 to Y.Z., and 32170716 to M.L.), the National Research and Development Program of China (2021YFA0805800 to A.J.Z. and M.L.), the Ministry of Education Key Laboratory of Cell Proliferation and Differentiation (to A.J.Z.), the Peking-Tsinghua Center for Life Sciences (to A.J.Z. and M.L.), and the Natural Science Foundation of Sichuan Province (2025ZNSFSC0988 to Y.Z.). Y.Z. was a Peking University President's Scholarship Awardee. Y.Z. and S.L. were supported by Boya Postdoctoral Fellowships.

AUTHOR CONTRIBUTIONS

J.L., Y.Z., J.P., M.L., and A.J.Z. designed the study. J.L. and J.P. performed experiments involving fly genetics, lipid staining, immunofluorescence staining, ROS level measurement, immunoprecipitation, and immunoblotting analyses using materials from fly tissues or cultured cells with the help of Y.P. J.L. prepared samples for mass spectrum analyses and performed molecular docking studies and mice studies. Y.Z. performed MST, *in vitro* pull-down, and ubiquitination analyses. W.Y. and M.G. collected glioma patient samples and normal brain tissue samples and performed relevant data analyses. J.L. and Y.X. purified proteins and conducted ATP-binding assays, *in vitro* HNEylation assays, *in vitro* ATPase activity assays, quantitative real-time PCR, and cell proliferation experiments with the help of J.Y. J.L., Y.Z., J.P., S.L., Y.L., X.G., W.D., X.Y., and M.L. analyzed data. A.J.Z. and J.L. wrote the paper with the help of M.L. and Y.Z.

DECLARATION OF INTERESTS

The authors declare no competing interests.

STAR★METHODS

Detailed methods are provided in the online version of this paper and include the following:

SUPPLEMENTAL INFORMATION

Supplemental information can be found online at https://doi.org/10.1016/j.molcel.2025.08.009.

Received: November 2, 2024
Revised: April 11, 2025
Accepted: August 6, 2025
Published: August 26, 2025

REFERENCES

1. Sies, H., and Jones, D.P. (2020). Reactive oxygen species (ROS) as pleiotropic physiological signalling agents. Nat. Rev. Mol. Cell Biol. *21*, 363–383. https://doi.org/10.1038/s41580-020-0230-3.
2. Sies, H., Mailloux, R.J., and Jakob, U. (2024). Fundamentals of redox regulation in biology. Nat. Rev. Mol. Cell Biol. *25*, 701–719. https://doi.org/10.1038/s41580-024-00730-2.
3. Glorieux, C., Liu, S., Trachootham, D., and Huang, P. (2024). Targeting ROS in cancer: rationale and strategies. Nat. Rev. Drug Discov. *23*, 583–606. https://doi.org/10.1038/s41573-024-00979-4.
4. Luo, H., Chiang, H.H., Louw, M., Susanto, A., and Chen, D. (2017). Nutrient sensing and the oxidative stress response. Trends Endocrinol. Metab. *28*, 449–460. https://doi.org/10.1016/j.tem.2017.02.008.
5. Forman, H.J., and Zhang, H. (2021). Targeting oxidative stress in disease: promise and limitations of antioxidant therapy. Nat. Rev. Drug Discov. *20*, 689–709. https://doi.org/10.1038/s41573-021-00233-1.
6. Hayes, J.D., Dinkova-Kostova, A.T., and Tew, K.D. (2020). Oxidative stress in cancer. Cancer Cell *38*, 167–197. https://doi.org/10.1016/j.ccell.2020.06.001.
7. Itoh, K., Chiba, T., Takahashi, S., Ishii, T., Igarashi, K., Katoh, Y., Oyake, T., Hayashi, N., Satoh, K., Hatayama, I., et al. (1997). An Nrf2/small Maf heterodimer mediates the induction of phase II detoxifying enzyme genes through antioxidant response elements. Biochem. Biophys. Res. Commun. *236*, 313–322. https://doi.org/10.1006/bbrc.1997.6943.
8. Meister, A. (1983). Selective modification of glutathione metabolism. Science *220*, 472–477. https://doi.org/10.1126/science.6836290.
9. Olzmann, J.A., and Carvalho, P. (2019). Dynamics and functions of lipid droplets. Nat. Rev. Mol. Cell Biol. *20*, 137–155. https://doi.org/10.1038/s41580-018-0085-z.
10. Mathiowetz, A.J., and Olzmann, J.A. (2024). Lipid droplets and cellular lipid flux. Nat. Cell Biol. *26*, 331–345. https://doi.org/10.1038/s41556-024-01364-4.
11. Bailey, A.P., Koster, G., Guillermier, C., Hirst, E.M.A., MacRae, J.I., Lechene, C.P., Postle, A.D., and Gould, A.P. (2015). Antioxidant role for

lipid droplets in a stem cell niche of *Drosophila*. Cell *163*, 340–353. https://doi.org/10.1016/j.cell.2015.09.020.

12. Ramosaj, M., Madsen, S., Maillard, V., Scandella, V., Sudria-Lopez, D., Yuizumi, N., Telley, L., and Knobloch, M. (2021). Lipid droplet availability affects neural stem/progenitor cell metabolism and proliferation. Nat. Commun. *12*, 7362. https://doi.org/10.1038/s41467-021-27365-7.
13. Ioannou, M.S., Jackson, J., Sheu, S.H., Chang, C.L., Weigel, A.V., Liu, H., Pasolli, H.A., Xu, C.S., Pang, S., Matthies, D., et al. (2019). Neuron-astrocyte metabolic coupling protects against activity-induced fatty acid toxicity. Cell *177*, 1522–1535.e14. https://doi.org/10.1016/j.cell.2019.04.001.
14. Liu, L., Zhang, K., Sandoval, H., Yamamoto, S., Jaiswal, M., Sanz, E., Li, Z., Hui, J., Graham, B.H., Quintana, A., et al. (2015). Glial lipid droplets and ROS induced by mitochondrial defects promote neurodegeneration. Cell *160*, 177–190. https://doi.org/10.1016/j.cell.2014.12.019.
15. Liu, L., MacKenzie, K.R., Putluri, N., Maletić-Savatić, M., and Bellen, H.J. (2017). The glia-Neuron lactate shuttle and elevated ROS promote lipid synthesis in neurons and lipid droplet accumulation in glia via APOE/D. Cell Metab. *26*, 719–737.e6. https://doi.org/10.1016/j.cmet.2017.08.024.
16. Goodman, L.D., Ralhan, I., Li, X., Lu, S., Moulton, M.J., Park, Y.J., Zhao, P., Kanca, O., Ghaderpour Taleghani, Z.S., Jacquemyn, J., et al. (2024). Tau is required for glial lipid droplet formation and resistance to neuronal oxidative stress. Nat. Neurosci. *27*, 1918–1933. https://doi.org/10.1038/s41593-024-01740-1.
17. Haynes, P.R., Pyfrom, E.S., Li, Y., Stein, C., Cuddapah, V.A., Jacobs, J.A., Yue, Z., and Sehgal, A. (2024). A neuron-glia lipid metabolic cycle couples daily sleep to mitochondrial homeostasis. Nat. Neurosci. *27*, 666–678. https://doi.org/10.1038/s41593-023-01568-1.
18. Byrns, C.N., Perlegos, A.E., Miller, K.N., Jin, Z., Carranza, F.R., Manchandra, P., Beveridge, C.H., Randolph, C.E., Chaluvadi, V.S., Zhang, S.L., et al. (2024). Senescent glia link mitochondrial dysfunction and lipid accumulation. Nature *630*, 475–483. https://doi.org/10.1038/s41586-024-07516-8.
19. Broadfield, L.A., Pane, A.A., Talebi, A., Swinnen, J.V., and Fendt, S.M. (2021). Lipid metabolism in cancer: New perspectives and emerging mechanisms. Dev. Cell *56*, 1363–1393. https://doi.org/10.1016/j.devcel.2021.04.013.
20. Bensaad, K., Favaro, E., Lewis, C.A., Peck, B., Lord, S., Collins, J.M., Pinnick, K.E., Wigfield, S., Buffa, F.M., Li, J.L., et al. (2014). Fatty acid uptake and lipid storage induced by HIF-1α contribute to cell growth and survival after hypoxia-reoxygenation. Cell Rep. *9*, 349–365. https://doi.org/10.1016/j.celrep.2014.08.056.
21. Cheng, X., Geng, F., Pan, M., Wu, X., Zhong, Y., Wang, C., Tian, Z., Cheng, C., Zhang, R., Puduvalli, V., et al. (2020). Targeting DGAT1 ameliorates glioblastoma by increasing fat catabolism and oxidative stress. Cell Metab. *32*, 229–242.e8. https://doi.org/10.1016/j.cmet.2020.06.002.
22. Nam, H.J., Kim, Y.E., Moon, B.S., Kim, H.Y., Jung, D., Choi, S., Jang, J.W., Nam, D.H., and Cho, H. (2021). Azathioprine antagonizes aberrantly elevated lipid metabolism and induces apoptosis in glioblastoma. iScience *24*, 102238. https://doi.org/10.1016/j.isci.2021.102238.
23. Minami, J.K., Morrow, D., Bayley, N.A., Fernandez, E.G., Salinas, J.J., Tse, C., Zhu, H., Su, B., Plawat, R., Jones, A., et al. (2023). CDKN2A deletion remodels lipid metabolism to prime glioblastoma for ferroptosis. Cancer Cell *41*, 1048–1060.e9. https://doi.org/10.1016/j.ccell.2023.05.001.
24. Zhang, Y., Lin, S., Peng, J., Liang, X., Yang, Q., Bai, X., Li, Y., Li, J., Dong, W., Wang, Y., et al. (2022). Amelioration of hepatic steatosis by dietary essential amino acid-induced ubiquitination. Mol. Cell *82*, 1528–1542.e10. https://doi.org/10.1016/j.molcel.2022.01.021.
25. Mohyeldin, A., Garzón-Muvdi, T., and Quiñones-Hinojosa, A. (2010). Oxygen in stem cell biology: a critical component of the stem cell niche. Cell Stem Cell *7*, 150–161. https://doi.org/10.1016/j.stem.2010.07.007.
26. Listenberger, L.L., Ostermeyer-Fay, A.G., Goldberg, E.B., Brown, W.J., and Brown, D.A. (2007). Adipocyte differentiation-related protein reduces the lipid droplet association of adipose triglyceride lipase and slows triacylglycerol turnover. J. Lipid Res. *48*, 2751–2761. https://doi.org/10.1194/jlr.M700359-JLR200.
27. Dalleau, S., Baradat, M., Guéraud, F., and Huc, L. (2013). Cell death and diseases related to oxidative stress: 4-hydroxynonenal (HNE) in the balance. Cell Death Differ. *20*, 1615–1630. https://doi.org/10.1038/cdd.2013.138.
28. Kaushik, S., and Cuervo, A.M. (2015). Degradation of lipid droplet-associated proteins by chaperone-mediated autophagy facilitates lipolysis. Nat. Cell Biol. *17*, 759–770. https://doi.org/10.1038/ncb3166.
29. Zhao, W., Zhang, Y., Lin, S., Li, Y., Zhu, A.J., Shi, H., and Liu, M. (2023). Identification of Ubr1 as an amino acid sensor of steatosis in liver and muscle. J. Cachexia Sarcopenia Muscle *14*, 1454–1467. https://doi.org/10.1002/jcsm.13233.
30. Chantranupong, L., Scaria, S.M., Saxton, R.A., Gygi, M.P., Shen, K., Wyant, G.A., Wang, T., Harper, J.W., Gygi, S.P., and Sabatini, D.M. (2016). The CASTOR proteins are arginine sensors for the mTORC1 pathway. Cell *165*, 153–164. https://doi.org/10.1016/j.cell.2016.02.035.
31. Wolfson, R.L., Chantranupong, L., Saxton, R.A., Shen, K., Scaria, S.M., Cantor, J.R., and Sabatini, D.M. (2016). Sestrin2 is a leucine sensor for the mTORC1 pathway. Science *351*, 43–48. https://doi.org/10.1126/science.aab2674.
32. Abu-Remaileh, M., Wyant, G.A., Kim, C., Laqtom, N.N., Abbasi, M., Chan, S.H., Freinkman, E., and Sabatini, D.M. (2017). Lysosomal metabolomics reveals V-ATPase- and mTOR-dependent regulation of amino acid efflux from lysosomes. Science *358*, 807–813. https://doi.org/10.1126/science.aan6298.
33. Perkins, L.A., Doctor, J.S., Zhang, K., Stinson, L., Perrimon, N., and Craig, E.A. (1990). Molecular and developmental characterization of the heat shock cognate 4 gene of Drosophila melanogaster. Mol. Cell. Biol. *10*, 3232–3238. https://doi.org/10.1128/mcb.10.6.3232-3238.1990.
34. Rosenzweig, R., Nillegoda, N.B., Mayer, M.P., and Bukau, B. (2019). The Hsp70 chaperone network. Nat. Rev. Mol. Cell Biol. *20*, 665–680. https://doi.org/10.1038/s41580-019-0133-3.
35. Goloudina, A.R., Demidov, O.N., and Garrido, C. (2012). Inhibition of HSP70: a challenging anti-cancer strategy. Cancer Lett. *325*, 117–124. https://doi.org/10.1016/j.canlet.2012.06.003.
36. Zensho, H., Nishida, A., Shimizu, M., Uchitomi, Y., and Yamawaki, S. (1998). Heat shock protein 72 restores cyclic AMP accumulation after heat shock in N18TG2 cells. Brain Res. *790*, 278–283. https://doi.org/10.1016/s0006-8993(98)00072-9.
37. Elefant, F., and Palter, K.B. (1999). Tissue-specific expression of dominant negative mutant *Drosophila* HSC70 causes developmental defects and lethality. Mol. Biol. Cell *10*, 2101–2117. https://doi.org/10.1091/mbc.10.7.2101.
38. Coyne, A.N., Lorenzini, I., Chou, C.C., Torvund, M., Rogers, R.S., Starr, A., Zaepfel, B.L., Levy, J., Johannesmeyer, J., Schwartz, J.C., et al. (2017). Post-transcriptional inhibition of Hsc70-4/HSPA8 expression leads to synaptic cycling defects in multiple models of ALS. Cell Rep. *21*, 110–125. https://doi.org/10.1016/j.celrep.2017.09.028.
39. Huang-Hobbs, E., Cheng, Y.T., Ko, Y., Luna-Figueroa, E., Lozzi, B., Taylor, K.R., McDonald, M., He, P., Chen, H.C., Yang, Y., et al. (2023). Remote neuronal activity drives glioma progression through SEMA4F. Nature *619*, 844–850. https://doi.org/10.1038/s41586-023-06267-2.
40. Laug, D., Glasgow, S.M., and Deneen, B. (2018). A glial blueprint for gliomagenesis. Nat. Rev. Neurosci. *19*, 393–403. https://doi.org/10.1038/s41583-018-0014-3.
41. Weller, M., Wick, W., Aldape, K., Brada, M., Berger, M., Pfister, S.M., Nishikawa, R., Rosenthal, M., Wen, P.Y., Stupp, R., et al. (2015). Glioma. Nat. Rev. Dis. Prim. *16*, 15017.
42. Wen, P.Y., and Reardon, D.A. (2016). Neuro-oncology in 2015: Progress in glioma diagnosis, classification and treatment. Nat. Rev. Neurol. *12*, 69–70. https://doi.org/10.1038/nrneurol.2015.242.

43. Chen, J., Ou, Y., Luo, R., Wang, J., Wang, D., Guan, J., Li, Y., Xia, P., Chen, P.R., and Liu, Y. (2021). SAR1B senses leucine levels to regulate mTORC1 signalling. Nature *596*, 281–284. https://doi.org/10.1038/s41586-021-03768-w.

44. Yang, W.S., SriRamaratnam, R., Welsch, M.E., Shimada, K., Skouta, R., Viswanathan, V.S., Cheah, J.H., Clemons, P.A., Shamji, A.F., Clish, C.B., et al. (2014). Regulation of ferroptotic cancer cell death by GPX4. Cell *156*, 317–331. https://doi.org/10.1016/j.cell.2013.12.010.

45. Conrad, M., Angeli, J.P.F., Vandenabeele, P., and Stockwell, B.R. (2016). Regulated necrosis: disease relevance and therapeutic opportunities. Nat. Rev. Drug Discov. *15*, 348–366. https://doi.org/10.1038/nrd.2015.6.

46. Doll, S., Freitas, F.P., Shah, R., Aldrovandi, M., da Silva, M.C., Ingold, I., Goya Grocin, A., Xavier da Silva, T.N., Panzilius, E., Scheel, C.H., et al. (2019). FSP1 is a glutathione-independent ferroptosis suppressor. Nature *575*, 693–698. https://doi.org/10.1038/s41586-019-1707-0.

47. Bersuker, K., Hendricks, J.M., Li, Z., Magtanong, L., Ford, B., Tang, P.H., Roberts, M.A., Tong, B., Maimone, T.J., Zoncu, R., et al. (2019). The CoQ oxidoreductase FSP1 acts parallel to GPX4 to inhibit ferroptosis. Nature *575*, 688–692. https://doi.org/10.1038/s41586-019-1705-2.

48. Stockwell, B.R. (2022). Ferroptosis turns 10: Emerging mechanisms, physiological functions, and therapeutic applications. Cell *185*, 2401–2421. https://doi.org/10.1016/j.cell.2022.06.003.

49. Zhou, J., Simon, J.M., Liao, C., Zhang, C., Hu, L., Zurlo, G., Liu, X., Fan, C., Hepperla, A., Jia, L., et al. (2022). An oncogenic JMJD6-DGAT1 axis tunes the epigenetic regulation of lipid droplet formation in clear cell renal cell carcinoma. Mol. Cell *82*, 3030–3044.e8. https://doi.org/10.1016/j.molcel.2022.06.003.

50. Dessi, S., Batetta, B., Pulisci, D., Spano, O., Cherchi, R., Lanfranco, G., Tessitore, L., Costelli, P., Baccino, F.M., and Anchisi, C. (1992). Altered pattern of lipid metabolism in patients with lung cancer. Oncology *49*, 436–441. https://doi.org/10.1159/000227088.

51. Saliakoura, M., Rossi Sebastiano, M., Pozzato, C., Heidel, F.H., Schnöder, T.M., Savic Prince, S., Bubendorf, L., Pinton, P., A Schmid, R., Baumgartner, J., et al. (2020). PLCγ1 suppression promotes the adaptation of KRAS-mutant lung adenocarcinomas to hypoxia. Nat. Cell Biol. *22*, 1382–1395. https://doi.org/10.1038/s41556-020-00592-8.

52. Guri, Y., Colombi, M., Dazert, E., Hindupur, S.K., Roszik, J., Moes, S., Jenoe, P., Heim, M.H., Riezman, I., Riezman, H., et al. (2017). mTORC2 promotes tumorigenesis via lipid synthesis. Cancer Cell *32*, 807–823.e12. https://doi.org/10.1016/j.ccell.2017.11.011.

53. Haney, M.S., Pálovics, R., Munson, C.N., Long, C., Johansson, P.K., Yip, O., Dong, W., Rawat, E., West, E., Schlachetzki, J.C.M., et al. (2024). APOE4/4 is linked to damaging lipid droplets in Alzheimer's disease microglia. Nature *628*, 154–161. https://doi.org/10.1038/s41586-024-07185-7.

54. Marschallinger, J., Iram, T., Zardeneta, M., Lee, S.E., Lehallier, B., Haney, M.S., Pluvinage, J.V., Mathur, V., Hahn, O., Morgens, D.W., et al. (2020). Lipid-droplet-accumulating microglia represent a dysfunctional and proinflammatory state in the aging brain. Nat. Neurosci. *23*, 194–208. https://doi.org/10.1038/s41593-019-0566-1.

55. Li, Y., Munoz-Mayorga, D., Nie, Y., Kang, N., Tao, Y., Lagerwall, J., Pernaci, C., Curtin, G., Coufal, N.G., Mertens, J., et al. (2024). Microglial lipid droplet accumulation in tauopathy brain is regulated by neuronal AMPK. Cell Metab. *36*, 1351–1370.e8. https://doi.org/10.1016/j.cmet.2024.03.014.

56. Xiong, W.C., Okano, H., Patel, N.H., Blendy, J.A., and Montell, C. (1994). repo encodes a glial-specific homeo domain protein required in the Drosophila nervous system. Genes Dev. *8*, 981–994. https://doi.org/10.1101/gad.8.8.981.

57. Luo, L., Liao, Y.J., Jan, L.Y., and Jan, Y.N. (1994). Distinct morphogenetic functions of similar small GTPases: Drosophila Drac1 is involved in axonal outgrowth and myoblast fusion. Genes Dev. *8*, 1787–1802. https://doi.org/10.1101/gad.8.15.1787.

58. Brigui, A., Hofmann, L., Argüelles, C., Sanial, M., Holmgren, R.A., and Plessis, A. (2015). Control of the dynamics and homeostasis of the *Drosophila* Hedgehog receptor Patched by two C2-WW-HECT-E3 Ubiquitin ligases. Open Biol. *5*, 150112. https://doi.org/10.1098/rsob.150112.

59. Port, F., Chen, H.M., Lee, T., and Bullock, S.L. (2014). Optimized CRISPR/Cas tools for efficient germline and somatic genome engineering in *Drosophila*. Proc. Natl. Acad. Sci. USA *111*, E2967–E2976. https://doi.org/10.1073/pnas.1405500111.

60. Liu, M., Liu, A., Wang, J., Zhang, Y., Li, Y., Su, Y., and Zhu, A.J. (2021). Competition between two phosphatases fine-tunes Hedgehog signaling. J. Cell Biol. *220*, e202010078. https://doi.org/10.1083/jcb.202010078.

61. Zhang, Y.L., Guo, H., Zhang, C.S., Lin, S.Y., Yin, Z., Peng, Y., Luo, H., Shi, Y., Lian, G., Zhang, C., et al. (2013). AMP as a low-energy charge signal autonomously initiates assembly of AXIN-AMPK-LKB1 complex for AMPK activation. Cell Metab. *18*, 546–555. https://doi.org/10.1016/j.cmet.2013.09.005.

62. Jiang, Y., Liu, T., Lee, C.H., Chang, Q., Yang, J., and Zhang, Z. (2020). The NAD^+-mediated self-inhibition mechanism of pro-neurodegenerative Sarm1. Nature *588*, 658–663. https://doi.org/10.1038/s41586-020-2862-z.

63. Wang, L.C., Liao, L.X., Lv, H.N., Liu, D., Dong, W., Zhu, J., Chen, J.F., Shi, M.L., Fu, G., Song, X.M., et al. (2017). Highly selective activation of heat shock protein 70 by allosteric regulation provides an insight into efficient neuroinflammation inhibition. EBioMedicine *23*, 160–172. https://doi.org/10.1016/j.ebiom.2017.08.011.

64. Zhou, C., Ma, L., Xu, H., Huo, Y., and Luo, J. (2022). Meningeal lymphatics regulate radiotherapy efficacy through modulating anti-tumor immunity. Cell Res. *32*, 543–554. https://doi.org/10.1038/s41422-022-00639-5.

STAR★METHODS

KEY RESOURCES TABLE

REAGENT or RESOURCE	SOURCE	IDENTIFIER
Antibodies		
Mouse anti-FLAG (WB: 1/1000)	Engibody Biotechnology	Cat# AT0022
Mouse anti-Myc (9B11) (WB: 1/2000)	Cell Signaling Technology	Cat# 2276S; RRID: AB_331783
Rabbit anti-β-Actin (WB: 1/1000)	ABclonal Technology	Cat# AC026; RRID: AB_2768234
Mouse anti-GST (B-14) (WB: 1/2000)	Santa Cruz Biotechnology	Cat# sc-138; RRID: AB_627677
Rabbit anti-4-HNE (WB: 1/1000; IF: 1/200)	Abcam	Cat# ab46545; RRID: AB_722490
Rabbit anti-PLIN2 (EPR3713) (WB: 1/1000)	Abcam	Cat# ab108323; RRID: AB_10863476
Guinea pig anti-PLIN2 (IP: 1/40)	PROGEN	Cat# GP40S; RRID: AB_1540416
Rabbit anti-HSPA8 (EP1531Y) (WB: 1/1000; IP: 1/20)	Abcam	Cat# ab51052; RRID: AB_880538
Rabbit anti-UBR1 (WB: 1/500)	Proteintech	Cat# 26069-1-AP; RRID: AB_2880360
Rabbit anti-UBR2 (WB: 1/1000)	Thermo Fisher	Cat# PA5-103823; RRID: AB_2853156
Rabbit anti-Cleaved Caspase 3 (Asp175) (WB: 1/1000; IHC: 1/100)	Cell Signaling Technology	Cat# 9661; RRID: AB_2341188
Rabbit anti-GFP (WB: 1/3000)	Zhang et al.[24]	N/A
Rabbit anti-*Drosophila* Plin2 (WB: 1/1000 for tissue samples and 1/3000 for *in vitro* assay samples)	Zhang et al.[24]	N/A
Rabbit anti-*Drosophila* Ubr1 (WB: 1/1000; IP: 1/20)	Zhang et al.[24]	N/A
HRP-conjugated Goat anti-Rabbit IgG (H+L) (WB: 1/10000)	ABclonal Technology	Cat# AS014; RRID: AB_2769854
HRP-conjugated Goat anti-Mouse IgG (H+L) (WB: 1/10000)	ABclonal Technology	Cat# AS003; RRID: AB_2769851
HRP-conjugated Donkey anti-Rabbit IgG (H+L) (IHC: 1/200)	ABclonal Technology	Cat# AS038; RRID: AB_2769848
Goat anti-Rabbit IgG (H + L), Alexa Fluor™ 488 (IF: 1/200)	Thermo Fisher	Cat# A-11008; RRID: AB_143165
Bacterial and Virus Strains		
DH10Bac competent cells	Beijing Zoman Biotechnology	Cat# ZK223
Trans1 T1 competent cells	TransGen Biotech	Cat# CD501
BL21 (DE3) competent cells	TransGen Biotech	Cat# CD601
Biological Samples		
Information about human samples, see Table S5	This paper	N/A
Chemicals, Peptides, and Recombinant Proteins		
Schneider's *Drosophila* medium	Thermo Fisher	Cat# 21720024
Sf-900 II SFM medium	Thermo Fisher	Cat# 10902096
Dulbecco's modified Eagle's medium (DMEM)	Thermo Fisher	Cat# C11995500BT
OPM-293 CD05 medium	OPM Biosciences	Cat# 81075-001
Fetal bovine serum	Cellmax	Cat# SA201.02
Puromycin	Sigma-Aldrich	Cat# 540411
Penicillin-Streptomycin	Thermo Fisher	Cat# 15140122
MG132	Sigma-Aldrich	Cat# SML1135
$CuSO_4$	Sigma-Aldrich	Cat# C1297
CellROX Deep Red	Thermo Fisher	Cat# C10422
BODIPY 493/503	Thermo Fisher	Cat# D3922
Nile Red	Sigma-Aldrich	Cat# 72485
DAPI	Thermo Fisher	Cat# D1306
IPTG	Amresco	Cat# 0487
Protease inhibitor cocktail	Gene-Protein Link	Cat# P10C01
PreScission protease	Cytiva	Cat# 27084301

(*Continued on next page*)

Continued

REAGENT or RESOURCE	SOURCE	IDENTIFIER
Trizma base (Tris)	JSENB	Cat# JS0159
Glycine	JSENB	Cat# JS0028
SDS	JSENB	Cat# JS0054
NP-40 (IGEPAL® CA-630)	Sigma-Aldrich	Cat# I8896
Triton X-100	Sigma-Aldrich	Cat# T8787
Tween-20	Sigma-Aldrich	Cat# P1379
3x FLAG peptide	Sigma-Aldrich	Cat# F4799
Magzol	Magen	Cat# R4801-02
N-acetyl-L-cysteine	Sigma-Aldrich	Cat# A7250
Trypan blue	Coolaber	Cat# SL7120
Hydrogen peroxide	Sigma-Aldrich	Cat# H433854
Tert-butyl hydroperoxide	Sigma-Aldrich	Cat# 458139
4-hydroxy-2-nonenal	MedChemExpress	Cat# HY-113466
Quercetin	Sigma-Aldrich	Cat# PHR1488
Silica MagBeads	Aladdin	Cat# S8099
Fmoc-β-Leu	Rhawn	Cat# R003672
Fmoc-β-Ala	Rhawn	Cat# R010370
Standard chow diet with 10 kcal% fat	Research Diets	Cat# D12450B
Critical Commercial Assays		
Agarose anti-GFP	Vector Laboratories	Cat# MB-0732
Agarose anti-FLAG	Sigma-Aldrich	Cat# A2220
Pierce™ glutathione agarose	Thermo Fisher	Cat# 16100
Dynabeads™ Protein A Immunoprecipitation Kit	Thermo Fisher	Cat# 10006D
Dynabeads™ Protein G Immunoprecipitation Kit	Thermo Fisher	Cat# 10007D
Adenosine 5′-triphosphate agarose	Sigma-Aldrich	Cat# A6888
Ni-NTA agarose	QIAGEN	Cat# 30210
Bradford Protein Assay Kit	Beyotime	Cat# P0006
CNBR-activated Sepharose beads 4B	Cytiva	Cat# 17043001
Superose 6 Increase 10/300 GL column	Cytiva	Cat# 29091596
Lipofectamine™ 2000 Transfection Reagent	Thermo Fisher	Cat# 11668019
Cellfectin II reagent	Thermo Fisher	Cat# 10362100
PowerUp SYBR Green Master Mix	Thermo Fisher	Cat# A25776
Eastep Super Total RNA Extraction Kit	Promega	Cat# LS1040
Eastep RT Master Mix Kit	Promega	Cat# LS2050
BCA protein assay kit	Thermo Fisher	Cat# 23250
Enhanced ECL kit	Biodragon	Cat# BF06053
Monolith LabelFree capillaries	NanoTemper	Cat# MO-Z022
Malachite Green Phosphate Detection Kit	Beyotime Biotechnology	Cat# S0196
GSH and GSSG Assay Kit	Beyotime Biotechnology	Cat# S0053
VECTASHIELD® Antifade Mounting Medium	Vector Laboratories	Cat# H-1200
Deposited Data		
Original western blot images	This paper	https://doi.org/10.17632/5mrzngzfyh.1
Experimental Models: Cell Lines		
Drosophila Schneider 2 (S2)	ATCC	CRL-1963; RRID: CVCL_Z232
Spodoptera fruiperda 9 (Sf9)	ATCC	CRL-1711; RRID: CVCL_0549
HEK293S	ATCC	CRL-3022; RRID: CVCL_A785
HEK293T	ATCC	CRL-3216; RRID: CVCL_0063
MO3.13	BNCC	BNCC360263; RRID: CVCL_D357

(*Continued on next page*)

Continued

REAGENT or RESOURCE	SOURCE	IDENTIFIER
U-87MG	ATCC	HTB-14; RRID: CVCL_0022
U-251MG	CCTCC	GDC0093; RRID: CVCL_0021
T98G	ATCC	CRL-1690; RRID: CVCL_0556
GL261	DSMZ	ACC-802; RRID: CVCL_Y003
Experimental Models: Organisms/Strains		
Drosophila, $w^{1118}{}_{iso}$; 2_{iso}; 3_{iso} (iso31)	Bloomington Drosophila Stock Center	BDSC Cat# 5905
Drosophila, UAS-*Ubr1-RNAi*	Bloomington Drosophila Stock Center	BDSC Cat# 31374
Drosophila, *repo*-Gal4	Xiong et al.[56]	N/A
Drosophila, UAS-*plin2-RNAi*	Tsinghua Fly Center	THFC Cat# THU1031
Drosophila, UAS-*LacZ*	Bloomington Drosophila Stock Center	BDSC Cat# 1776
Drosophila, UAS-*w-RNAi*	Tsinghua Fly Center	THFC Cat# THU0583
Drosophila, UAS-*FLAG-Ubr1*^{CA}	This paper	N/A
Drosophila, UAS-*Hsc70-4*^{C267A}-*Myc*	This paper	N/A
Drosophila, *Ubr1*$^{C1703A,\ C1706A}$ knock-in (Denoted as *Ubr1*^{CA})	Zhang et al.[24]	N/A
Drosophila, *Hsc70-4*^{C267A} knock-in	This paper	N/A
Drosophila, *Ubr1*^{KO}	Zhang et al.[24]	N/A
Drosophila, *insc*-Gal4	Luo et al.[57]	N/A
Drosophila, *elav*^{C155}-Gal4	Bloomington Drosophila Stock Center	BDSC Cat# 458
Drosophila, UAS-*Lamp1-RNAi*	Tsinghua Fly Center	THFC Cat# THU5208
Drosophila, UAS-*Hsc70-3-RNAi*	Bloomington Drosophila Stock Center	BDSC Cat# 32402
Drosophila, UAS-*Hsc70-4-RNAi*	Bloomington Drosophila Stock Center	BDSC Cat# 28709
Drosophila, UAS-*Hsc70-4*^{D206S} (Denoted as UAS-*Hsc70-4*^{CD})	Bloomington Drosophila Stock Center	BDSC Cat# 5844
Mus musculus, BALB/c nude	Charles River Laboratories International	N/A
Mus musculus, C57BL6/J	Charles River Laboratories International	N/A
Oligonucleotides		
gRNAs for generating *Hsc70-4*^{C267A} knock-in, see Table S3	This paper	N/A
Information about small interfering RNAs, see Table S3	This paper	N/A
Primers for quantitative real-time PCR, see Table S3	This paper	N/A
Primers for cloning, see Table S3	This paper	N/A
Recombinant DNA		
Plasmid: *pAct-Myc-Ub*^{K48}	Brigui et al.[58]	N/A
Plasmid: *pcDNA3.1*	Zhang et al.[24]	N/A
Plasmid: *pcDNA3.1-hHSPA8*^{C267A}	This paper	N/A
Plasmid: *pEG Bacmam-Ubr1-GFP*	Zhang et al.[24]	N/A
Plasmid: *pEG Bacmam-plin2-GFP*	This paper	N/A
Plasmid: *pEG Bacmam-Hsc70-4*	This paper	N/A
Plasmid: *pEG Bacmam-Hsc70-4*^{C267A}	This paper	N/A

(*Continued on next page*)

Continued		
REAGENT or RESOURCE	SOURCE	IDENTIFIER
Plasmid: *pEG Bacmam-Hsc70-4^{CD}*	This paper	N/A
Plasmid: *pGST-parallel2.1-Hsc70-4*	This paper	N/A
Plasmid: *pGST-parallel2.1-Hsc70-4^{C267A}*	This paper	N/A
Plasmid: *pGST-parallel2.1-mHspa8*	This paper	N/A
Plasmid: *pGST-parallel2.1-mHspa8^{C267A}*	This paper	N/A
Plasmid: *pGST-parallel2.1-hHSPA8*	This paper	N/A
Plasmid: *pGST-parallel2.1-hHSPA8^{C267A}*	This paper	N/A
Plasmid: *pKS* (*Hsc70-4^{C267A}* knock-in) *(donor)*	This paper	N/A
Plasmid: *pMT-plin2-GFP*	Zhang et al.[24]	N/A
Plasmid: *pMT-FLAG-Ubr1*	Zhang et al.[24]	N/A
Plasmid: *pMT-FLAG-Ubr1-N*	Zhang et al.[24]	N/A
Plasmid: *pMT-Ubr1-C-Myc*	Zhang et al.[24]	N/A
Plasmid: *pMT-FLAG-Hsc70-4*	This paper	N/A
Plasmid: *pMT-Hsc70-4-Myc*	This paper	N/A
Plasmid: *pMT-Hsc70-4^{CD}-Myc*	This paper	N/A
Plasmid: *pMT-FLAG-Ubr1^{CA}*	This paper	N/A
Plasmid: *pUAST-FLAG-Ubr1^{CA} (mini-white)*	This paper	N/A
Plasmid: *pUAST-Hsc70-4^{C267A}-Myc (mini-white)*	This paper	N/A
Plasmid: *pSIN-GFP*	This paper	N/A
Plasmid: *pSIN-GFP-HSPA8^{C267A}*	This paper	N/A
Software and Algorithms		
Adobe Illustrator CC	Adobe	https://www.adobe.com/cn/products/illustrator.html
Applied Biosystems 7500 Real-Time PCR Software	Thermo Fisher	https://www.thermofisher.com/cn/zh/home/technical-resources/software-downloads/applied-biosystems-7500-real-time-pcr-system.html
BD FACS Diva™ Software	BD Biosciences	https://www.bdbiosciences.com/
FlowJo Software	FlowJo	https://www.flowjo.com/
GraphPad Prism 8	GraphPad	http://www.graphpad.com
Image J 1.53	National Institutes of Health	https://imagej.nih.gov/ij/download.html
Leica LAS X	Leica Microsystems	https://www.leica-microsystems.com
MO.Control	NanoTemper	https://www.nanotempertech.com/
Photoshop CS5	Adobe	https://www.adobe.com/cn/products/photoshop.html
Other		
BD LSR Fortessa™ Cell Analyzer	BD Biosciences	https://www.bdbiosciences.com/
BioSpec 94/20 9.4T	Bruker Corporation	https://www.bruker.com
Hamilton syringe	Hamilton Company	Cat# 7653-01
Leica DM IL LED microscope	Leica Microsystems	https://www.leica-microsystems.com
Leica TCS SP8 inverted confocal microscope	Leica Microsystems	https://www.leica-microsystems.com
Monolith NT.LabelFree	NanoTemper	https://www.nanotempertech.com/
Standard brain stereotactic frame	RWD Life Sciences	https://www.rwdls.com
Tri-Carb 3110TR Low Activity Liquid Scintillation Analyzer	PerkinElmer	https://www.perkinelmer.com
40x, 1.3 NA oil-immersion objective	Leica Microsystems	https://www.leica-microsystems.com
63x, 1.4 NA oil-immersion objective	Leica Microsystems	https://www.leica-microsystems.com

EXPERIMENTAL MODEL AND STUDY PARTICIPANT DETAILS

Fly manipulation

Fly culture and crosses were carried out according to standard procedures. Unless otherwise specified, flies were raised on standard medium (45 g agar, 155 g yeast, 516 g glucose, 258 g sucrose and 858 g cornmeal in 8.5 L water). For larval oxidative stress treatment, a modified standard procedure was used.[11] Briefly, eggs were collected at 25°C for 3 hours using the apple juice/agar plates (22.5% apple juice, 1.25% sucrose, 1% low melting point agar in PBS) supplemented with yeast paste. After 24 hours of growth, early first-instar larvae (0 hour after larval hatching) were transferred to standard medium for continued development. Mid third-instar larvae (80 hours after larval hatching at 25°C) were then transferred to agarose medium (0.5% low melting-point agarose in PBS) containing either H_2O_2 (0.5% v/v, Sigma-Aldrich, 323381) or tBH (100 mM, Sigma-Aldrich, 458139) for pro-oxidant treatment, or transferred to agarose medium in an O_2 cabinet calibrated to 2.5% oxygen and 97.5% nitrogen for hypoxia treatment. Control larvae were transferred to agarose medium in normoxic conditions (20.9% oxygen). After 16-hour treatment, late third-instar larvae (96 hours after larval hatching at 25°C) were collected for subsequent experiments. For *ex vivo* 4-HNE treatment, late third-instar larvae (96 hours after larval hatching at 25°C) were dissected to remove excess tissues, retaining the brain. The tissues were incubated with 100 μM 4-HNE (MedChemExpress, HY-113466) in Schneider's *Drosophila* medium (Thermo Fisher, 21720024) for an hour at 30°C, followed by lipid staining.

Hsc70-4^{C267A} knock-in flies were generated via CRISPR/Cas9-mediated homologous recombination as previously described.[59] Briefly, a *pCFD1* plasmid with guide RNA (gRNA) and the donor vector *pKS* (*Hsc70-4*^{C267A} knock-in) were co-injected into nos-Cas9 fly embryos. Genomic DNA PCR and sequencing were used to identify positive lines. Note that the *Hsc70-4*$^{C267A/C267A}$ knock-in flies were backcrossed into the w^{1118}_{iso}; 2_{iso}; 3_{iso} (iso31) genetic background for six generations before analysis. UAS-*FLAG-Ubr1*^{CA} and UAS-*Hsc70-4*^{C267A}*-Myc* transgenic flies were generated using Φ31-mediated transgenic integration.

All fly lines used in this study are listed in the key resources table. Detailed genotypes and experimental conditions are provided in Table S4. Unless otherwise stated, male *Drosophila* larvae were used in all experiments.

Cell lines

Drosophila Schneider 2 (S2) cells (ATCC, CRL-1963) were cultured at 25°C in Schneider's *Drosophila* medium (Thermo Fisher, 21720024) supplemented with 10% fetal bovine serum (FBS) (Cellmax, SA201.02) and 1% penicillin/streptomycin (Thermo Fisher, 15140122). *Spodoptera frugiperda* 9 (Sf9) cells (ATCC, CRL-1711) were maintained at 27°C in Sf-900 II SFM medium (Thermo Fisher, 10902096). HEK293T (ATCC, CRL-1573), MO3.13 (BNCC, BNCC360263), U87MG (ATCC, HTB-14), U251MG (CCTCC, GDC0093), T98G (ATCC, CRL-1690), GL261 (DSMZ, ACC-802) cells were cultured at 37°C with 5% CO_2 in Dulbecco's modified Eagle's medium (DMEM) (Thermo Fisher, C11995500BT) supplemented with 10% FBS and 1% penicillin/streptomycin. HEK293S cells (ATCC, CRL-3022) were cultured at 37°C with 5% CO_2 in OPM-293 CD05 medium (OPM Biosciences, 81075-001) supplemented with 1% FBS and 1% penicillin/streptomycin.

GBM mouse models

All experimental procedures involving mice were performed in compliance with animal protocols approved by the Institutional Animal Care and Use Committee (IACUC) of Peking University. Mice were housed in colony cages with a 12-hour/12-hour light/dark cycle and provided with free access to water and food.

Orthograft models were generated using female athymic nude mice (6-8 weeks old; Charles River Laboratories International) injected with human U87 cells or male C57BL6/J mice (6-8 weeks old; Charles River Laboratories International) injected with mouse GL261 cells. Experiments were initiated following a 7-day acclimation period after the mice were received. For the intracranial tumor model, U87 or GL261 cells stably expressing *GFP* or *HSPA8*^{C267A}*-GFP* (1×10^5) were suspended in 2 μL PBS and stereotaxically injected into brains of anesthetized mice fixed in a stereotactic frame. Coordinates for injection were 2 mm lateral and 1mm posterior from the bregma, with a depth of 3 mm beneath the dura. A Hamilton syringe (Hamilton, 7653-01) was used to deliver the cell suspension. Mice were monitored daily, and were considered to have reached the overall survival endpoint and sacrificed when their body weight loss exceeded 15% from their peak weight.

Human sample information

Tumor samples from glioma patients and normal brain tissues, collected from cerebral autopsy specimens of non-cancer individuals, were provided by Beijing Children's Hospital. The use of these tissues was approved by the Institutional Review Board of Beijing Children's Hospital. Detailed information about human samples is summarized in Table S5.

METHOD DETAILS

Antibodies

The antibodies used in this study, including their respective dilutions, are listed in the key resources table. Primary antibodies against HSPA8 (Abcam, Cat# 51052), PLIN2 (Abcam, Cat# 108323), UBR1 (Proteintech, Cat# 26069-1-AP) and UBR2 (Thermo Fisher,

Cat# PA5-103823) exhibited cross-species reactivity to human and mouse orthologs. The antibody against β-Actin (ABclonal, Cat# AC026) showed cross-species reactivity with human, mouse and fly orthologs.

Cell transfection and drug treatments

Drosophila S2 cells were transfected using the calcium phosphate-based method as previously described,[60] except for siRNA experiments, Lipofectamine™ 2000 Transfection Reagent (Thermo Fisher, 11668019) was used according to the manufacturer's instructions. siRNA sequences are listed in Table S3.

For transfection in mammalian cells, Lipofectamine™ 2000 Transfection Reagent was used unless otherwise stated. To generate stable U87 or GL261 cell lines, HEK293T cells were co-transfected with the expression vector, packaging plasmid psPAX2, and envelope plasmid pMD2.G for lentiviral packaging. 48 hours after transfection, conditioned media were harvested and added to infect U87 or GL261 cells. 72 hours later, transduced cells were collected and sorted by fluorescence activated cell sorting. Stable U87 or GL261 cell lines derived from single clones were expanded and maintained for subsequent experiments.

For starvation treatment in S2 cells, cells were washed once with PBS, and then incubated in Krebs-Ringers bicarbonate buffer (KRB, 10 mM glucose, 0.5 mM magnesium chloride, 4.52 mM potassium chloride, 120.7 mM sodium chloride, 0.7 mM dibasic sodium phosphate, 1.5 mM monobasic sodium phosphate, 15 mM sodium bicarbonate, 5.4 mM calcium chloride at pH 7.4) for one hour.

For oxidative stress treatment in S2 cells, cells were washed once with PBS and then subjected to either 16-hour hypoxia (2.5% oxygen) or cultured in S2 medium (or KRB buffer for concurrent starvation treatment) containing H_2O_2, tBH or 4-HNE at specified concentrations for one hour. To inhibit the degradation of Plin2 in experiments detecting Ubr1-Plin2 interaction, 20 μM proteasome inhibitor MG132 (Sigma-Aldrich, SML1135) was added to S2 cells during starvation or oxidative stress treatments. For oxidative stress treatment in MO3.13 cells, cells were washed once with PBS and then cultured in DMEM medium containing 250 μM H_2O_2 for one hour.

Lipid staining and immunofluorescence staining

Lipid staining for the late third-instar larval brain was carried out as previously described with modifications.[11] Briefly, larval pelts were cleaned of excess tissues except for the brain. Tissues were fixed in 4% paraformaldehyde for 30 minutes, washed three times with PBS, and incubated with 1 μg/mL BODIPY (Thermo Fisher, D3922) and 10 μg/mL DAPI (Thermo Fisher, D1306) for 15 minutes. After washing the larval pelts three times with PBS, larval brains were excised and mounted in Vectashield Antifade Mounting Medium (Vector Laboratories, H-1200). For MO3.13 cells, cells were transfected with indicated plasmids. 48 hours after transfection, cells were treated with 250 μM H_2O_2 for one hour. BODIPY staining was performed as described.[61] Briefly, cells on coverslips were fixed in 4% paraformaldehyde for 10 minutes, washed three times with PBS, and incubated with 1 μg/mL BODIPY and 10 μg/mL DAPI for 10 minutes. After washing, slides were mounted for imaging. For lipid staining of xenograft tumor tissues, cryosections (8 μm thickness) were air-dried and fixed in formaldehyde for one hour. Slides were then washed three times with PBS, and incubated with 50 μg/mL Nile red and 10 μg/mL DAPI for 15 minutes. After washing, slides were mounted and imaged.

For immunofluorescence staining in fly larval brains, standard procedure was used with modifications.[11] Briefly, larval pelts were cleaned of excess tissues except for the brain. Tissues were fixed in 4% paraformaldehyde for 30 minutes and washed three times with PBS. Tissues were blocked for one hour in PBS containing 0.1% Triton X-100 (PBSTr) and 0.2% BSA. Larval pelts were incubated with primary antibody overnight at 4°C, washed three times with PBSTr, and then incubated with secondary antibody for 2 hours at room temperature. After three additional PBSTr washes, tissues were stained with 10 μg/mL DAPI for 15 minutes, washed with PBSTr buffer three times, and larval brains were excised and mounted. Antibody details, including dilutions, are listed in the key resources table.

Image acquisition, analysis and quantification

Fluorescence images were acquired using a Leica TCS SP8 confocal system using 40x or 63x oil-immersion objective. Minor image adjustment (brightness and/or contrast) was performed within linear ranges in Adobe Photoshop CS5 when necessary. Control and experiment conditions were processed using identical parameters. Figures were assembled in Adobe Illustrator CC.

Fluorescence intensity quantifications for BODIPY, CellROX, and 4-HNE in larval brains, as well as Nile red in xenograft tumor tissues, were performed using confocal images acquired under identical settings for each probe. Mean pixel intensity was calculated using NIH ImageJ software. All images were analyzed in their raw format as acquired without post-acquisition modifications. Each data point represents the fluorescence intensity of an entire ventral nerve cord from one larva, or corresponds to one field of view from a tumor cryosection.

Reactive oxygen species (ROS) level measurement

CellROX Deep Red (Thermo Fisher, C10422) staining was performed on late third-instar larval brains to detect ROS levels. Briefly, the larval pelts were cleaned of excess tissues except brain, washed three times with PBS, and incubated in S2 medium containing 5 μM CellROX Deep Red for one hour at 30°C. After being fixed in 4% paraformaldehyde for 30 minutes and washed three times with PBS, tissues were stained with 10 μg/mL DAPI for 15 minutes. After three additional washes with PBS, larval brains were excised, mounted and imaged.

The ratio of reduced glutathione to oxidized glutathione (GSH/GSSG) was analyzed to assess ROS levels. Briefly, GSH and GSSG concentrations of *Drosophila* larval brains, *Drosophila* S2 cells, mammalian cells, and xenograft tumor tissues were quantified using a GSH/GSSG detection kit (Beyotime, S0053) according to the manufacturer's instructions. The GSH/GSSG ratio was calculated to evaluate oxidative stress.

Immunoprecipitation and immunoblotting analyses

Immunoblotting analyses were performed using standard protocols.[60] Mammalian cells, *Drosophila* S2 cells, or third-instar larval brains (about 100 larvae for each group) were homogenized and lysed in RIPA lysis buffer [50 mM Tris-HCl (Sigma-Aldrich, T1530), 150 mM NaCl, 0.1% SDS, 1% NP-40 (IGEPAL® CA-630, Sigma-Aldrich, I8896), pH 8.0] supplemented with 1% EDTA-free protease inhibitor cocktail (Gene-Protein Link, P10C01) unless otherwise stated. Lysates were mixed with SDS sample buffer (250 mM Tris-HCl, 10% 2-mercaptoethanol, 20% glycerol, 6% SDS and 0.02% bromophenol blue, pH 6.8), and boiled for 6 minutes at 98°C. After centrifugation, the supernatant was resolved via SDS-PAGE. Proteins on gels were then transferred to PVDF membranes using standard wet transfer methods. PVDF membranes were blocked in 5% non-fat milk in PBS containing 0.05% Tween 20 (PBSTw), and probed with indicated primary antibodies in PBSTw containing 2.5% non-fat milk overnight at 4°C. After washing three times in PBSTw, blots were incubated with HRP-conjugated secondary antibodies in PBSTw containing 2.5% non-fat milk for 2 hours at room temperature. Membranes were washed three times in PBSTw, and signals were detected using an enhanced ECL kit (Biodragon, BF06053). Images were captured with a Li-cor Odyssey Fc Imaging System, cropped, and adjusted for brightness/contrast using Image Studio and Adobe Photoshop CS5, ensuring no non-linear alterations. Antibody dilutions and sources are listed in the key resources table.

For immunoprecipitation, mammalian cells, *Drosophila* S2 cells, xenograft tumor tissues, or patient tissues were homogenized and lysed in NP40 lysis buffer (50 mM Tris-HCl, 150 mM NaCl, 1% NP-40, pH 8.0) supplemented with 1% protease inhibitor at 4°C for 30 minutes. For transfection-based immunoprecipitation, cells were plated in 6-well plates and transfected with transgene-expressing vectors or siRNAs. 48-72 hours after transfection, cells were harvested, lysed, and centrifuged. Cleared supernatants of cell lysates were incubated with washed GFP (Vector Laboratories, MB-0732) or FLAG (Sigma-Aldrich, A2220) antibody-conjugated agarose at 4°C for 12 hours with rotation. For immunoprecipitation of endogenous proteins, cell or tissue extracts were cleared with multiple rounds of centrifugation to remove insoluble components. Cleared supernatants were incubated at 4°C with respective antibodies for 12 hours, and with protein A/G beads (Thermo Fisher, 10006D/10007D) for another 8 hours. The beads were washed three times with NP40 lysis buffer, and immunoprecipitated proteins were eluted by boiling in SDS sample buffer at 98°C for 6 minutes. For input control, a fraction of supernatant was reserved prior to bead addition, mixed with SDS sample buffer, and boiled at 98°C for 6 minutes for parallel analysis. For experiments assessing Ubr1-Plin2 or UBR1/2-PLIN2 interactions, S2 cells or MO3.13 cells were treated with 20 μM proteasome inhibitor MG132 (Sigma-Aldrich, SML1135) for 6 hours before harvest to inhibit the degradation of Plin2.

For *in vitro* cell-free pull-down assays, 2 μg purified *Drosophila* GFP-Ubr1 and 2 μg purified Plin2 protein were incubated in NP40 lysis buffer supplemented with indicated amino acid concentrations at 4°C for 4 hours. The GFP-antibody conjugated beads were added to the reaction mixture and incubated at 4°C for 8 hours with rotation. The beads were washed three times with NP40 lysis buffer, and immunoprecipitated proteins were eluted by boiling in SDS sample buffer at 98°C for 6 minutes. For input control, a fraction of the reaction mixture was reserved prior to bead addition, mixed with SDS sample buffer, and boiled at 98°C for 6 minutes for parallel analysis. Samples were resolved by SDS-PAGE and analyzed via immunoblotting.

Ubiquitination analysis

Ubiquitination assays were performed with hot-lysis-extracted protein lysates to remove noncovalently associated proteins, as previously described.[60] Briefly, transfected *Drosophila* S2 cells were treated with 20 μM MG132 in cultured medium for 6 hours before harvest to prevent ubiquitinated proteins from degradation. Harvested cells were resuspended in denaturing buffer (50 mM Tris-HCl, 0.5 mM EDTA, 1% SDS, pH 7.5) supplemented with protease inhibitors, and hot-lysed by boiling at 98°C for 6 minutes. Lysates were centrifuged, and supernatants were diluted 1:3 with RIPA lysis buffer to reduce SDS concentration. Diluted lysates were subjected to immunoprecipitation to capture specific ubiquitinated proteins. Samples were resolved by SDS-PAGE and analyzed via immunoblotting.

For *in vitro* cell-free ubiquitination assays, 2 μg purified Plin2 protein was incubated with 15 μg ubiquitin, 550 ng UBE1 (E1), 850 ng HR2B (E2), and 2 μg purified *Drosophila* GFP-Ubr1 in 1x ubiquitin reaction buffer supplemented with 12.5 mM Mg^2+-ATP and varying concentrations of amino acids at 37°C for an hour. Reactions were terminated by boiling in SDS sample buffer at 98°C for 6 minutes.

Protein purification

For the purification of GST-Hsc70-4 and GST-Hsc70-4^{C267A}, fusion proteins were expressed in BL21 (DE3) *E. coli* (TransGen Biotech, CD601) and induced with 0.5 mM IPTG at 37°C for 6 hours. Cells were homogenized and lysed via sonication in pull-down lysis buffer (50 mM Tris, 1mM EDTA, 100mM NaCl, pH 7.4). Supernatants were then collected for purification. GST-tagged proteins were purified by glutathione agarose (Thermo Fisher, 16100) and eluted with 10 mM GSH in equilibration buffer (50 mM Tris and 150 mM NaCl, pH 8.0). Protein concentration was measured using the Bradford Protein Assay Kit (Beyotime, P0006).

For the purification of *Drosophila* Ubr1 proteins, a standard procedure was used with modifications.[62] Briefly, pEG BacMam vectors expressing GFP-tagged Ubr1 were transformed into DH10Bac (Beijing Zoman Biotechnology, ZK223) to generate bacmids. Sf9 cells were then transfected with these bacmids using Cellfectin II reagent (Thermo Fisher, 10362100), and recombinant baculoviruses were subsequently produced. HEK293S cells infected with recombinant baculovirus were initially cultured at 37°C for 8-12 hours, and then cultured at 30°C in medium supplemented with 10 mM sodium butyrate. Note that the addition of H_2O_2 (200 μM), tBH (200 μM), quercetin (10 μM, Sigma-Aldrich, PHR1488) or 4-HNE (10 μM), and the co-expression of fly *Hsc70-4, Hsc70-4*^{CD} or *Hsc70-4*^{C267A} were conducted during this process. Following harvest, cells were lyzed in lysis buffer (50 mM HEPES pH 8.0, 300 mM NaCl, 15% glycerol, 5 mM β-mercaptoethanol) containing protease inhibitors and 2 μg/mL DNase. After sonication on ice, the supernatant was collected and incubated with Ni-NTA beads (QIAGEN, 30210) for 6 hours at 4°C, followed by washing with five column volumes of 20 mM imidazole and elution with 250 mM imidazole. GFP-Ubr1 proteins were further purified via gel filtration chromatography on a Superose 6 Increase 10/300 GL column (Cytiva, 29091596), with final elution in wash buffer to remove contaminated proteins. For Plin2 protein purification, recombinant GFP-Plin2 protein expressed in HEK293S cells was purified with anti-GFP nanobody-coupled CNBR-activated Sepharose beads (Cytiva, 17043001) for 2 hours at 4°C. The resin was rinsed with wash buffer (25 mM HEPES pH 7.5, 300 mM NaCl, and 5 mM β-mercaptoethanol) and treated with PreScission protease (5:1 w/w ratio, Cytiva, 27084301) at 4°C overnight to cleave and elute Plin2 protein. Protein concentration was measured using the Bradford Protein Assay Kit.

Quantitative real-time PCR

Total RNA from *Drosophila* third-instar larval brains or cultured cells was isolated using the Eastep Super Total RNA Extraction Kit (Promega, LS1040). cDNA synthesis was carried out with the Eastep RT Master Mix Kit (Promega, LS2050). For quantitative analysis, real-time PCRs were performed on an Applied Biosystems 7500 Real-time PCR system (Thermo Fisher, USA) with PowerUp SYBR Green Master Mix (Thermo Fisher, A25776). Transcript levels were quantified via the comparative CT method, and statistical comparisons between groups were conducted using GraphPad Prism 8 (GraphPad Software, La Jolla, CA, USA). Three biological replicates were analyzed, each measured in triplicate.

Microscale thermophoresis (MST) assay

MST assays were performed to measure amino acid-binding affinities of *Drosophila* Ubr1 protein purified from HEK293S cells using a Monolith NT.LabelFree instrument (NanoTemper) following standard procedures. Recombinant Ubr1 protein, fused with a GFP tag at the C-terminus, served as a fluorescent label for real-time monitoring. Protein purity was confirmed via Coomassie blue staining, and concentrations were determined using the Bradford Protein Assay Kit. For binding assays, Ubr1 protein was held constant at 50 nM, while amino acids were serially diluted in twofold steps from 1 mM to 1/32768 mM (16-point dilution series). After thoroughly mixed, samples were incubated at 25°C for 40 minutes to stabilize Ubr1-amino acid interactions. Subsequently, samples were loaded into Monolith LabelFree capillaries (NanoTemper, Cat# MO-Z022), which were then inserted into the Monolith NT.LabelFree instrument in ascending order of amino acid concentration. Fluorescence signals from GFP-tagged Ubr1 were monitored using the Monolith NT. LabelFree instrument. Data obtained from samples with different amino acid concentrations were analyzed using MO.Control and GraphPad Prism 8 software, with binding curves generated from three independent biological replicates.

Molecular docking assay

Molecular docking analysis was conducted to characterize the interaction between 4-HNE and *Drosophila* Hsc70-4 protein (UniProt ID: P11147). The structural model of Hsc70-4 was obtained from the AlphaFoldDB database and preprocessed using Schrödinger software's Protein Preparation Wizard module (Schrödinger Maestro 13.5). For the ligand, the 2D structure of 4-HNE (PubChem CID: 5283344) was retrieved from the PubChem database and converted into 3D chiral conformations via Schrödinger software's LigPrep module. Potential binding sites between the protein and ligand were predicted using Schrödinger's SiteMap module, followed by the Receptor Grid Generation module of the Schrödinger software to define the most appropriate enclosing box to wrap the predicted binding site. Through these processes, the active site of Hsc70-4 that can be modified by 4-HNE was obtained.

The interaction between preprocessed 4-HNE and the active site of Hsc70-4 was simulated using Schrödinger's Covalent Docking module to model potential adduct formation driven by 4-HNE's reactivity. To refine the protein-ligand complex, energy minimization was performed with the Minimize module, identifying the conformation with the lowest binding free energy.

Mass spectrum (MS) analysis

For liquid chromatography-mass spectrometry/mass spectrometry (LC-MS/MS) identification of the Ubr1 interacting proteins and the posttranslational modifications of Hsc70-4, samples were resolved by SDS-PAGE, and the protein bands of interest were excised, reduced with 10 mM dithiothreitol, and alkylated using 55mM iodoacetamide, each for one hour. Gel pieces were subjected to in-gel digestion overnight with 10 ng/μL trypsin. The resulting peptides were extracted twice with 5% formic acid and 50% acetonitrile, dried via vacuum centrifugation, and resuspended in 0.1% formic acid in water (Solvent A) prior to LC-MS/MS analysis.

For the identification of the Ubr1 interacting proteins, resuspended peptides in Solvent A were loaded onto a 100μm x 2 cm precolumn, and separated on a 75 μm x 15 cm capillary column equipped with a laser-pulled sprayer, both packed in-house with Luna 3 μm C18(2) bulk packing material (Phenomenex, USA). Chromatographic separation was carried out on an Easy nLC 1000 system

(Thermo Scientific, USA) under the following conditions: a gradient starting at 5% Solvent B (0.1% formic acid in 80% acetonitrile) and increasing to 35% over 60 minutes, followed by a rapid rise to 75% Solvent B over 4 minutes, and a final hold at 75% Solvent B for 10 minutes. The flow rate was maintained at 300 nL/minute. Eluted peptides were sprayed into a Velos Pro Orbitrap Elite mass spectrometer (Thermo Scientific, USA) equipped with a nano-ESI source. The mass spectrometer was operated in data-dependent mode with a full MS scan (375–1600 M/z) in FT mode at a resolution of 120000, followed by CID (collision induced dissociation) MS/MS scans on the 10 most abundant ions of the initial MS scan. Automatic gain control (AGC) targets were 1e6 ions for Orbitrap scans and 5e4 for MS/MS scans. Dynamic exclusion parameters were configured with an isolation window of 2 m/z, a repeat count of 1, a repeat duration of 25 seconds, and an exclusion duration of 25 seconds.

For the identification of the modified peptides of Hsc70-4, the samples were separated using a loading column (100 μm × 2 cm) and a C18 separating capillary column (75 μm × 15 cm) packed in-house with Luna 3 μm C18(2) bulk packing material (Phenomenex, USA). Mobile phases consisted of Solvent A and Solvent B were driven and controlled by a Dionex Ultimate 3000 RPLC nano system (Thermo Fisher, USA). The LC gradient started with 2% Solvent B for 8 minutes, followed by an increase to 44% Solvent B over 60 minutes, and a rapid increase to 99% Solvent B in 5 minutes. For the samples analyzed by Orbitrap Fusion LUMOS Tribrid Mass Spectrometer, the precursors were ionized using an EASY-Spray ionization source (Thermo Fisher, USA). Ionization parameters included a source voltage of +2.0 kV compared to ground, and an inlet capillary temperature of 320°C. Survey scans of peptide precursors were collected in the Orbitrap from 350-1800 Th, with an AGC target of 400,000, a maximum injection time of 50 ms, RF lens at 30%, and a resolution of 120,000 at 200 m/z. Monoisotopic precursor selection was enabled for peptide isotopic distributions, precursors of z = 2-8 were selected for data-dependent MS/MS scans, with 3-second cycle time, and dynamic exclusion of 15 seconds with a ±10 ppm window set around the precursor monoisotope.

The LC-MS/MS data processing was carried out using Thermo Proteome Discoverer 2.4. A *Drosophila melanogaster* protein databasedownloaded from uniprot.org (version 2019-11-08) served as the reference for protein identification. Carbomidomethylation of Cys was set as a fixed modification, while oxidation of Met and HNEylation of Cys were included as variable modifications. Mass tolerance was set at 10 ppm for precursor ions, and 0.02 Da for fragmentations. Maximum missed cleavages were set to 2. To valide peptide spectral matches (PSM), the Percolator algorithm was used, filtering results at a 1% false discovery rate (FDR) based on q-values.

Untargeted metabolomic analysis

Untargeted metabolomic profiling of oxidative stress-treated larval brains was conducted by Biotree Biotech Co., Ltd. (Shanghai, China). Raw data were acquired under both positive and negative ion modes, and then converted to the mzXML format using ProteoWizard. Data were processed with an in-house program developed using R and based on XCMS for peak detection, extraction, alignment, and integration. Metabolites were authenticated by searching Biotree DB (v2.1), an in-house MS2 database, with validation requiring a MS2 score greater than 0.3.

In vitro ATP affinity assay

The binding capacity of recombinant Hsc70-4 and Hsc70-4^{C267A} mutant for ATP was measured using ATP-linked agarose beads (Sigma, A6888). Briefly, Hsc70-4 or Hsc70-4^{C267A} was pre-incubated with 1 mM 4-HNE in PBS for an hour at 37°C. After treatment, the buffer was replaced with ATP binding buffer (10 mM Tris-HCl, 5 mM $MgCl_2$, pH 7.5), and the ATP-linked beads were added to the mixture. Binding reactions were allowed to proceed for 2 hours at 4°C with gentle rotation. After centrifugation, the supernatant was removed, and the beads were washed three times with NP40 lysis buffer. Bound proteins were eluted by boiling the beads in SDS sample buffer for 5 minutes. The extent of Hsc70-4 bound to the beads was determined via SDS-PAGE.

In vitro ATPase activity assay

Recombinant *Drosophila* Hsc70-4 or Hsc70-4^{C267A} proteins in TBS was pre-incubated with varying concentrations of 4-HNE for an hour at 37°C. Subsequently, 2.5 mM ATP was added, and the reaction mixture was further incubated for 3 hours at 37°C. The ATPase activity of Hsc70-4 or Hsc70-4^{C267A} was quantified by measuring inorganic phosphate released during ATP hydrolysis using the malachite green-based colorimetric assay (Beyotime, S0196), adapted from a previously described protocol.[63] Absorbance values were converted to inorganic phosphate concentrations using a sodium phosphate standard curve, with the amount of inorganic phosphate directly correlated to ATPase activity.

Cell proliferation assay

Different glioma cell lines were seeded in 12-well plates at a density of 1×10^4 cells per well on day 0. For drug treatment, 1 mM N-acetylcysteine (NAC; Sigma-Aldrich, A7250) was added to the culture medium and replenished daily. After digestion, cells were stained with 0.4% trypan blue staining solution (Coolaber, SL7120) to distinguish viable cells. Number of cells were counted using a Coulter Counter at fixed time points over a 6-day period.

Tumor volume measurement

Tumor volume was measured using T2-weighted rapid acquisition with relaxation enhancement (RARE) images on a BioSpec 94/20 MRI device. The acquisition parameters included an echo time (TE) of 10 ms and a repetition time (TR) of 3000 ms. A RARE factor of

16 was applied, and the number of average (NA) was set to 4. Each scan captured 25 image slices with a thickness of 0.5-mm and in-plane resolution of 150 μm. Tumor boundaries were determined from the T2 hyperintense regions in the brain, following previously reported methods.[64] Tumor volume was calculated using the formula: Tumor volume = length × width^2 × 0.523.

Immunohistochemistry

Tumor tissues were fixed in 4% PFA and embedded in paraffin. Immunohistochemistry staining was performed on 5 μm paraffin sections. Tissue slides were first placed in a 37°C oven overnight, and then deparaffinized in xylene three times (5 minutes each), followed by rehydration through a graded alcohol series (100%, 95%, 80% and 70%) with three 2-minute dips per concentration. After rinsing with distilled water (dH_2O) (three times 5-minute washed), endogenous peroxidase activity was quenched by immersing slides in 3% H_2O_2 for 10 minutes, followed by additional rinsing with dH_2O. Antigen retrieval was conducted by heating slides in pre-warmed 10 mM citrate buffer (pH 6.0) in a steamer for 30 minutes. After cooling, slides were rinsed with dH_2O and PBS. Non-specific binding was blocked with 2% BSA in 0.3% PBSTr for an hour at room temperature. Primary antibodies were applied and incubated overnight at 4°C. Slides were then washed with PBS and incubated with secondary antibodies at room temperature for two hours. After final wash with dH_2O, nuclei were counterstained with hematoxylin. Slides were dehydrated through a reverse alcohol gradient (70%, 80%, 95% and 100%) and cleared in xylene twice (5 minutes each). Mounted slides were imaged using a Leica DM IL LED microscope. Antibodies used in immunohistochemistry analyses and the dilution and source of each antibody are listed in the key resources table.

Amino acid-binding assay

For amino acid-binding assays, standard procedures were used to prepare amino acid-immobilized beads with some modifications.[29] Briefly, silica MagBeads (-NH2) (Aladdin, S8099) were incubated overnight at room temperature with Fmoc-β-Leu (Rhawn, R003672) or Fmoc-β-Ala (Adamas, R010370) in dimethyformamide (DMF) containing 1 mM EDC and 1 mM HOBt. Following washed in DMF, unreacted -NH2 groups on the beads were blocked by incubation with 150 mM acetic anhydride in DMF for 30 minutes at room temperature. After additional washes in DMF, the Fmoc group was removed by incubating the beads in 50% DBU for 2 hours. The resulting amino acid-immobilized beads were stored in methanol at 4°C. For amino acid-binding, amino acid-starved cell lysates were incubated with washed Leu-immobilized or Ala-immobilized beads overnight at 4°C with rotation. Immunoprecipitates were washed three times with NP40 lysis buffer, and eluted by boiling in SDS sample buffer and analyzed via immunoblotting.

QUANTIFICATION AND STATISTICAL ANALYSIS

Statistical analyses were performed using GraphPad Prism 8. Comparisons between two groups used a two-tailed Student's t-test, while comparisons involving three or more groups used one-way ANOVA followed by Dunnett's or Tukey's multiple comparison tests, as specified in figure legends. For experiments involving two independent variables, a two-way ANOVA followed by Bonferroni post-tests was used. Survival curves for mice or patients were analyzed using the Log rank test. Correlations were assessed via Spearman's rank analysis. The number of biological replicates, independent experiments, and relevant statistical tests for each dataset were detailed in the corresponding figure legends. Data are presented as standard error of the mean (SEM) unless otherwise noted. Statistical significance thresholds are indicated as follows: *$p < 0.05$. **$p < 0.01$. ***$p < 0.001$, with NS indicating not significant. All the experiments were independently replicated at least twice, with similar results observed across repetitions.